

Figure 8.8 Averaged P_{harm} of VIVACE with/without PTC for $K=1,000$ N/m.

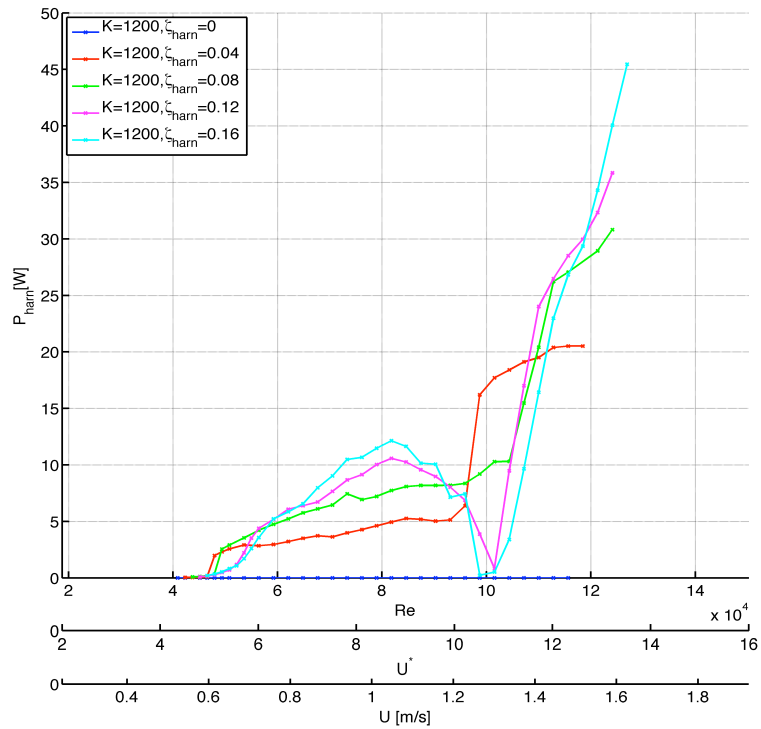


Figure 8.9. Averaged P_{harm} of VIVACE with/without PTC for $K=1,200$ N/m.

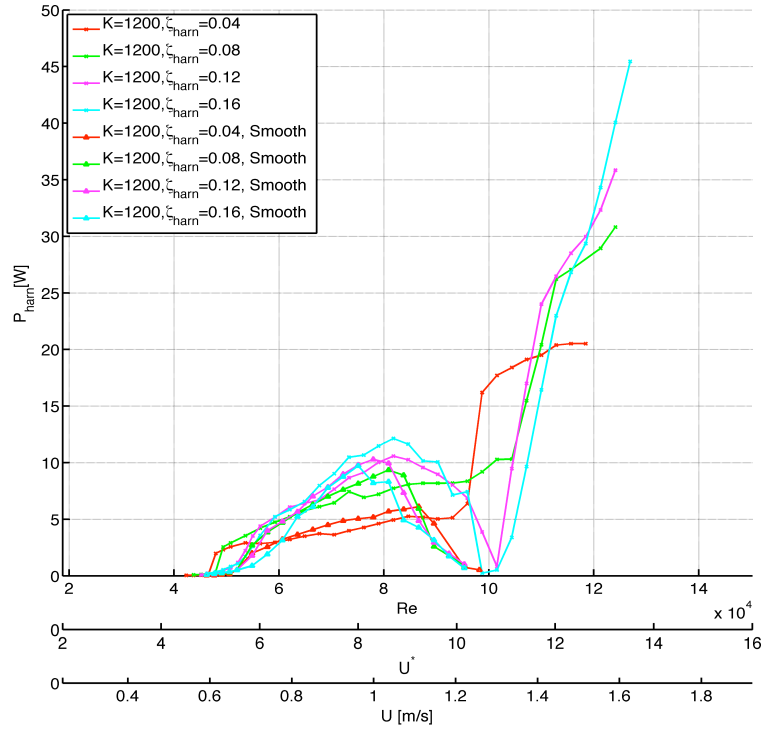


Figure 8.10. Averaged P_{harm} of VIVACE with/without PTC for $K=1,200$ N/m.

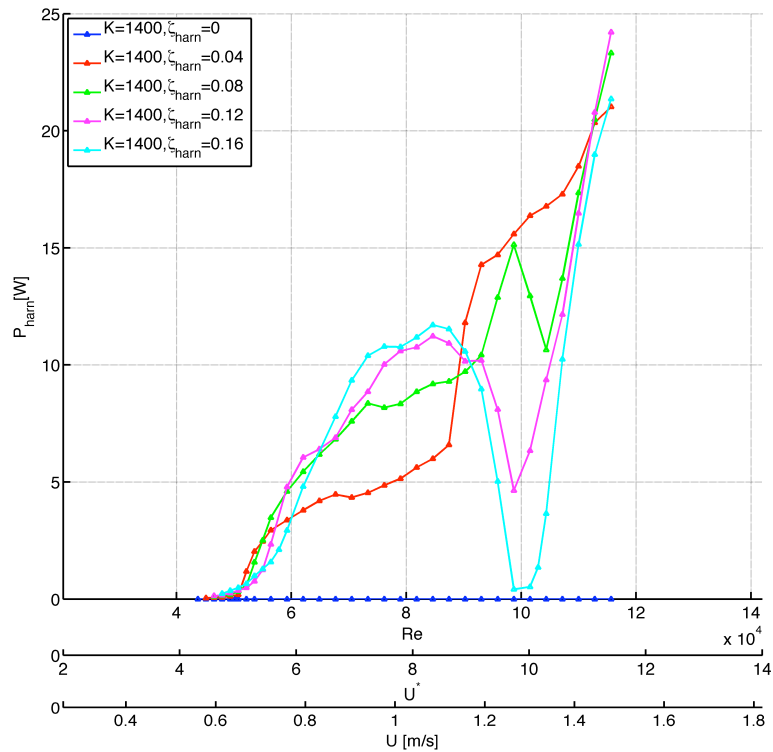


Figure 8.11. Averaged P_{harm} of VIVACE with/without PTC for $K=1,400$ N/m.

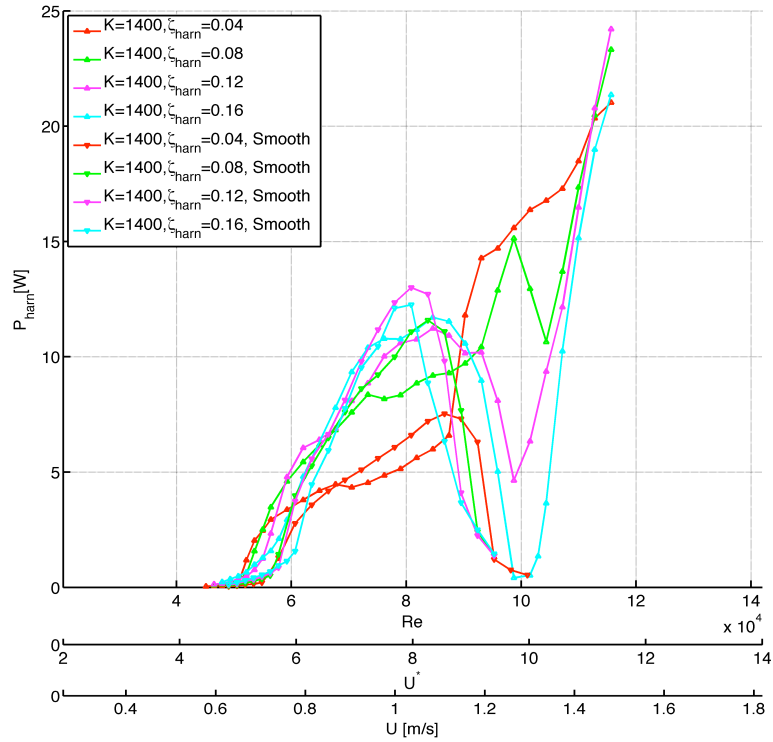


Figure 8.12. Averaged P_{harm} of VIVACE with/without PTC for $K=1,400$ N/m.

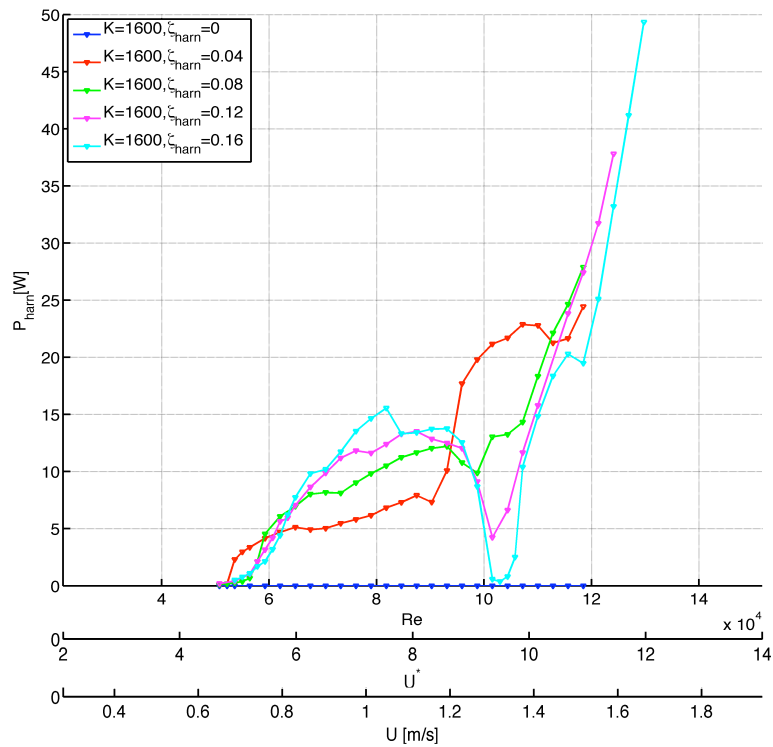


Figure 8.13. Averaged P_{harm} of VIVACE with PTC for $K=1,600$ N/m.

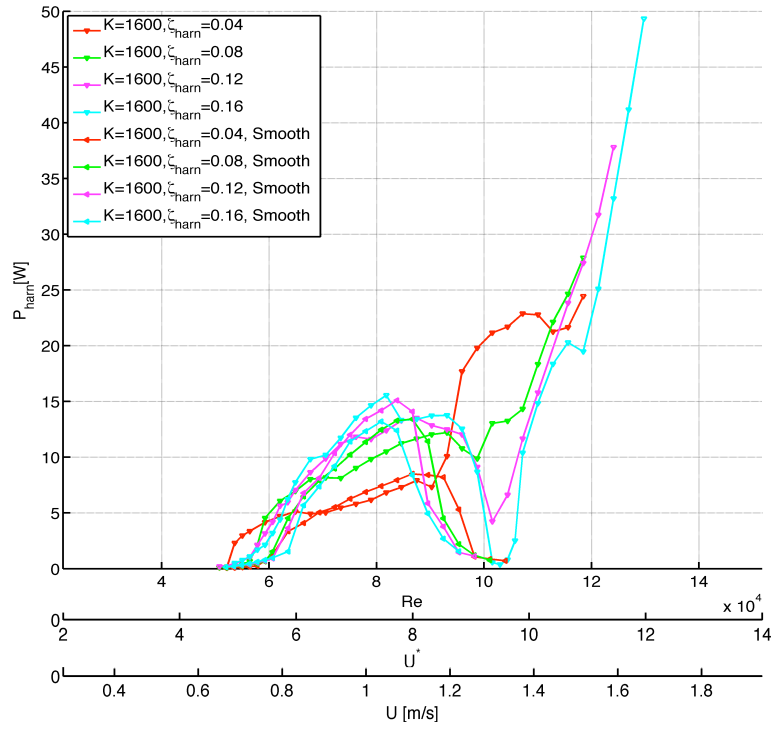


Figure 8.14. Averaged P_{harm} of VIVACE with/without PTC for $K=1,600$ N/m.

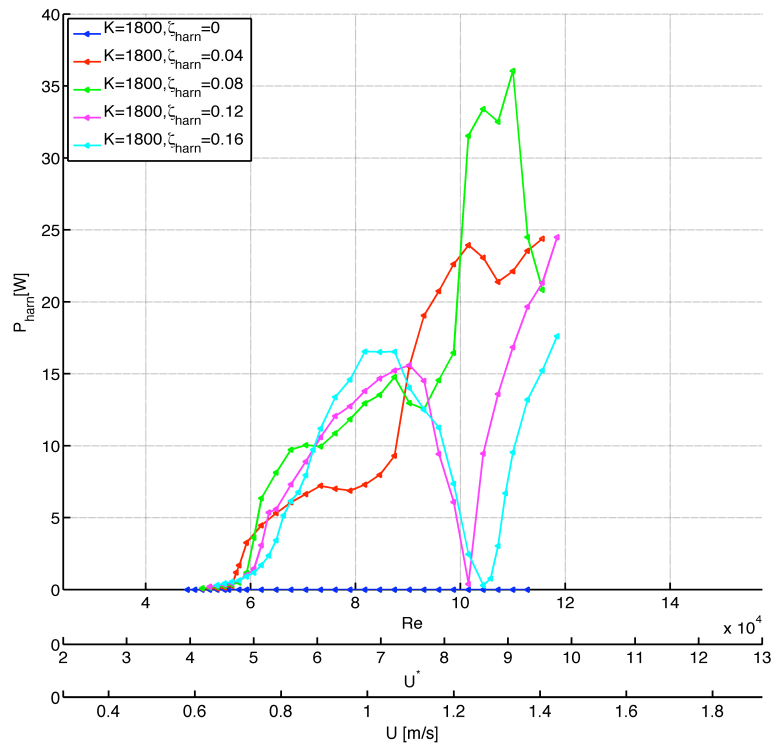


Figure 8.15. Averaged P_{harm} of VIVACE with PTC for $K=1,800$ N/m.

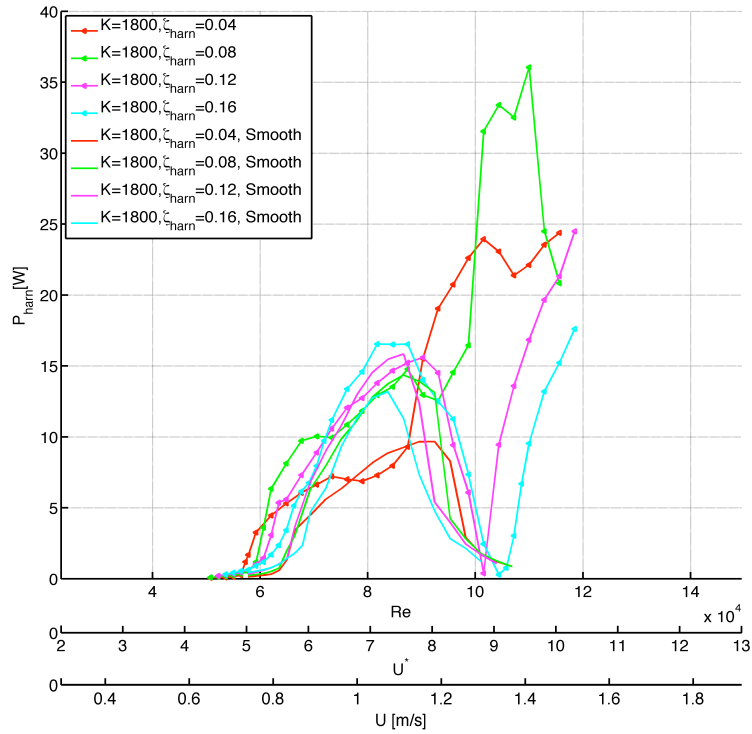


Figure 8.16. Averaged P_{harm} of VIVACE with/without PTC for $K=1,800$ N/m.

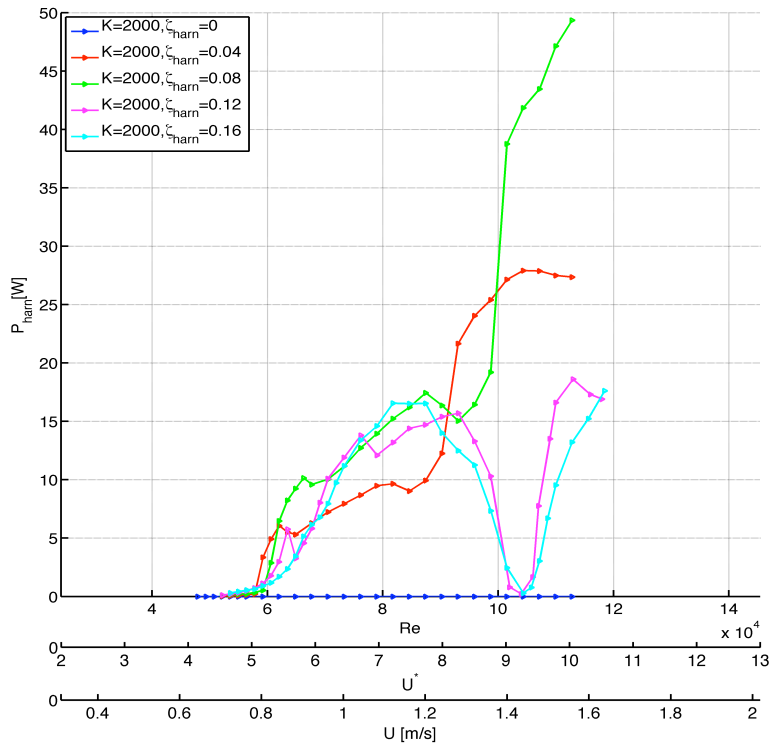


Figure 8.17. Averaged P_{harm} of VIVACE with/without PTC for $K=2,000$ N/m.

8.4. Optimal harnessed power envelop

Superposing the results of calculated harnessed power from Figure 8.7 to Figure 8.17, the optimal harnessed power curve is generated and is shown in Figure 8.18. The latter shows, that the optimal harnessed power curve can be divided into several zones characterized by different combinations of stiffness and damping values corresponding to specific flow speed ranges. In the lower flow speed range (0.36m/s ~ 0.82m/s), the maximum energy harnessing takes place at an optimum damping value of $\zeta_{\text{harn}} = 0.12$. As the flow speed is further increased (0.82m/s ~ 0.92m/s), a combination of slightly lower external damping ($\zeta_{\text{harn}} = 0.08$) yet with higher stiffness ($K = 2,000\text{N/m}$) corresponds to the optimum power generated. The next zone of optimal power profile falls in the flow speed range from 0.92m/s to 1.0m/s, which corresponds to $K = 2,000\text{N/m}$ and $\zeta_{\text{harn}} = 0.12$. The stiffness value remains the same in the subsequent optimal power zones and is combined with different values of ζ_{harn} . Next zone corresponds to the flow speed range from 1.0m/s to 1.2m/s and is associated with a higher value of $\zeta_{\text{harn}} = 0.16$. In the next zone (1.2m/s ~ 1.3m/s), the damping value ζ_{harn} used to generate the optimal power envelop drops to 0.04. More significantly, this flow speed range is where galloping begins to manifest strongly.

By applying PTC on the cylinder surface, the optimal harnessed power curve is extended to a broader flow velocity range from 0.38m/s to 1.45m/s with steeper slopes. As can be seen in Figure 8.19, the optimal harnessed power obtained with PTC is higher than that of the smooth cylinder within the range of flow velocity $0.4 \leq U \leq 1.14\text{m/s}$. For $U > 1.14\text{m/s}$, smooth cylinder amplitude drastically drops off due to de-synchronization, whereas under the same flow speed, the rough cylinder steps up its amplitude response favoring significantly higher power generation. It can further be noted that, the power dissipated shows a significant jump once flow velocity crosses a value of 1.2m/s, which is mostly synchronizing with the occurrence of galloping

The optimal power curve for VIVACE with PTC (rough cylinder) can be expressed as a second order of polynomial by curve-fitted as follows:

$$\text{Optimal power (W)} = 364.1U^2 - 363.85U + 95.569 \quad (8.8)$$

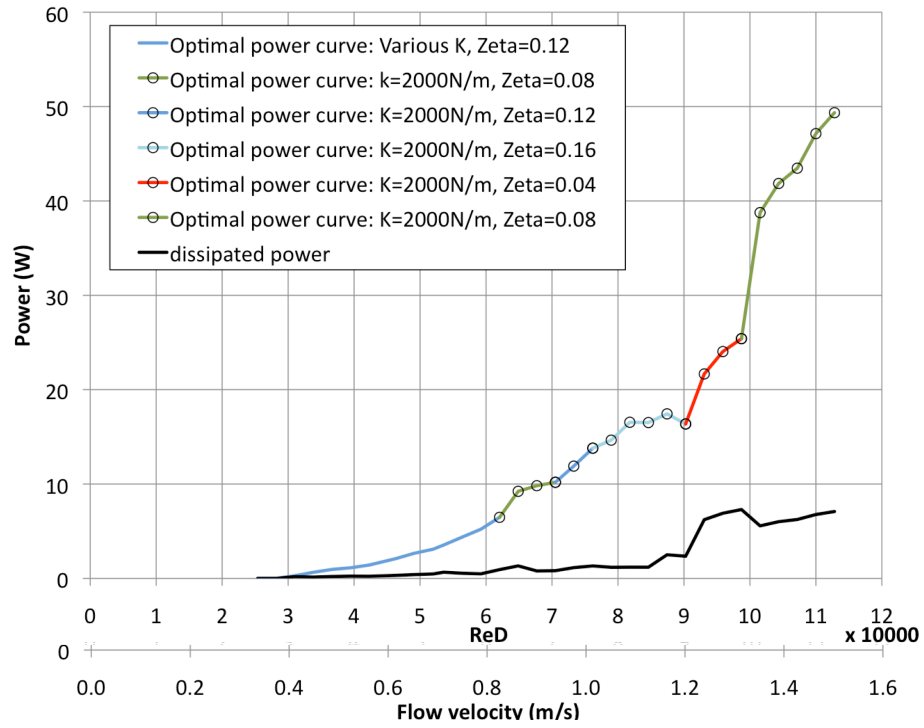


Figure 8.18. Optimal harnessed power envelope and corresponding dissipated power with information of system stiffness and damping (VIVACE with PTC).

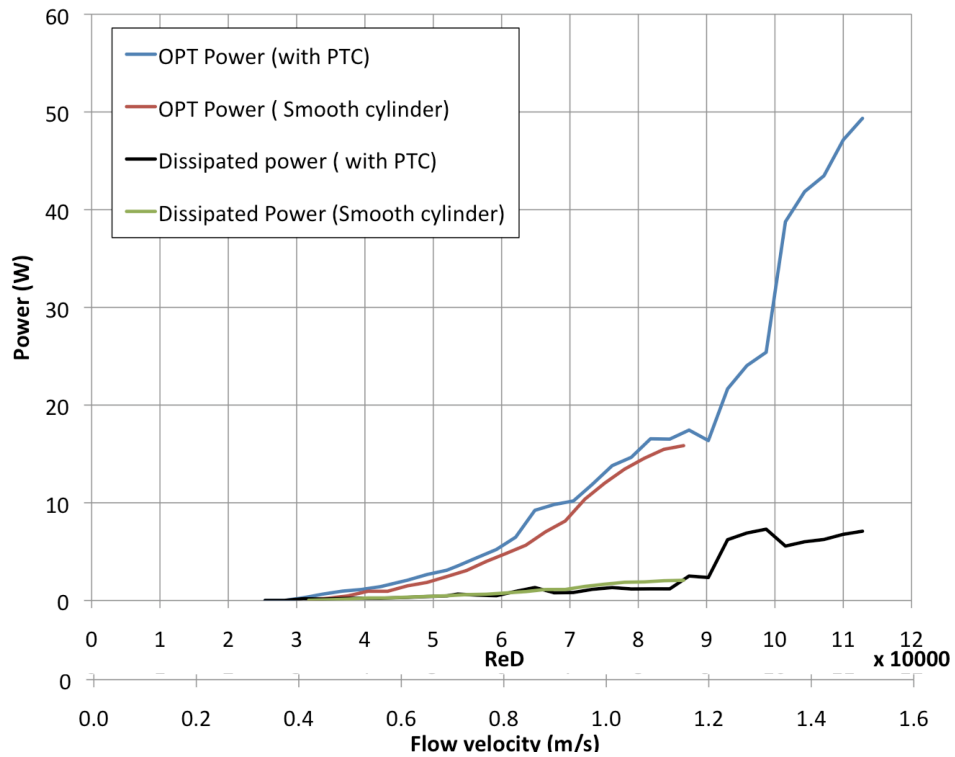


Figure 8.19. Optimal harnessed power envelope of VIVACE with PTC and without PTC.

8.5. VIVACE power density

Power density is an important metric that is useful when attempting to compare efficiency between power-producing devices, particularly renewable energy converters. It is especially important when space is constrained. The space area for VIVACE power plant is the first to be considered for power density calculation, and the association depends upon the overall size of VIVACE, which is in turn determined by the total number of cylinders implemented, as well as the inter-cylinder distances.

For a typical power calculation, a staggered configuration (see Figure 8.20) with $8*D$ inter-cylinder (center-to-center) spacing in the flow direction of flow and a $5*D$ inter-cylinder spacing in the transverse direction is selected, where D being the cylinder diameter. It is to be noted that, the spacing of this configuration not only fulfills but is greater than the required minimum of $4*D$ for minimal interference between the cylinders (Chen 1987; Zdravkovich 1997). Also, it is significantly larger than the in-flow and transverse clearance is of 2 diameters and 1 diameter, respectively, for a cylinder in VIV upstream from a fixed cylinder (Sumer and Fredsoe 1997). It needs to be emphasized that this configuration presented here is not an optimal for a VIVACE power plant because only VIV and transverse galloping are considered as the fluid forces exerted on the oscillating body in a single cylinder VIVACE. On the other hand, for multi-cylinder VIVACE, the effect of interference between cylinders will need to be considered as well, since additional excitation mechanisms like interference galloping and wake galloping are very likely to occur.

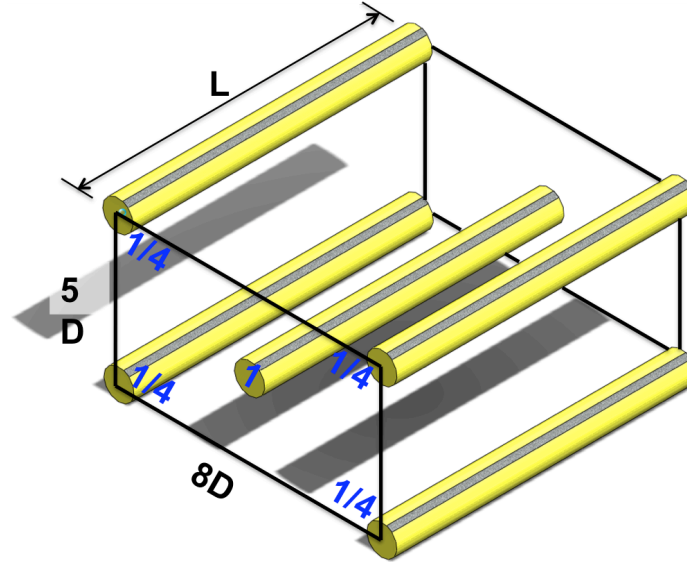


Figure 8.20. Configuration of cylinder deployment of the VIVACE converter.

For the selected VIVACE configuration, two cylinders are included in a volume of $40D^2L$. Applying it to the definition of power density, it yields

$$\text{Power density [W/m}^3\text{]} = \frac{2P_{\text{harm}}}{40D^2L} \quad (8.9)$$

Based on equation (8.9), the power density for VIVACE converter is calculated and is shown in Table 12.

For better understanding of the efficiency of the VIVACE converter, the calculated harnessed power (detailed in Section 8.2) is compared to the theoretical upper limit of harnessable power from a steady uniform flow. The upper limit of harnessed power was first derived by Betz (Cuevas et al. 2006). It can be calculated by letting U and U' be the flow velocity upstream and downstream of the VIVACE apparatus in a water channel, respectively. The mean flow velocity through cylinder is:

$$\tilde{U} = \frac{U + U'}{2} \quad (8.10)$$

Then, the mass flow rate through the cross-section is:

$$\begin{aligned}\dot{m}_{flow} &= \rho W_{water} D_{water} \tilde{U} \\ &= \rho W_{water} D_{water} \frac{U + U'}{2}\end{aligned}\quad (8.11)$$

where W_{water} is the width of the water channel and D_{water} is the water depth of the channel. The converted power from hydrokinetic to mechanical in the VIVACE converter is the difference between the hydrokinetic energy upstream and downstream of the device. Thus, we obtain:

$$P = \frac{1}{2} \dot{m}_{flow} (U^2 - U'^2) = \frac{1}{2} \rho W_{water} D_{water} U^3 \left(1 + \frac{U'}{U}\right) \left[1 - \left(\frac{U'}{U}\right)^2\right] \quad (8.12)$$

The maximum value of P occurs when $U^*/U = 1/3$. Thus the theoretical limit of harnessed power is:

$$\text{Theoretical upper limit (Max. Harnessable Power, } P_{max}) = \frac{16}{27} \frac{\rho}{2} W_{water} D_{water} U^3 \quad (8.13)$$

A ratio of harnessed power and fluid power in the water channel along with fluid power through the cylinder-projected area (DL) is presented in Table 12 as well. Definition of the above terms follows:

$$\text{Fluid Power in water channel} = \frac{1}{2} \rho W_{water} D_{water} U^3 \quad (8.14)$$

$$\text{Fluid power through the cylinder-projected area (DL)} = \frac{1}{2} \rho D L U^3 \quad (8.15)$$

where D and L represents the diameter and length of the cylinder. Conversion efficiency of VIVACE = $(P_{harn}/P_{limit}) \times 100\%$

TABLE 12. POWER GENERATED BY VIVACE CONVERTER WITH PTC

Flow velocity [m/s]	Reynolds number	Fluid channel power, P_{water} [W]	Max harnessable power, P_{max} [W]	min remaining flow power [W]	Fluid power in projected area, P_{DL} [W]	remaining fluid power [W]	vivace captured power [W]	Power harnessed by VI-VACE, P_{harm} [W]	Power Dissipated by VI-VACE, P_{dissip} [W]	Power density by VIVACE (W/m^3)	$(P_{harm}/P_{max})100\%$	$(P_{harm}/P_{DL})100\%$
0.40	8.25E+05	17.85	10.58	7.27	2.55	2.09	0.46	0.28	0.18	1.94	2.65	10.99
0.43	1.07E+06	23.17	13.73	9.44	3.31	2.52	0.79	0.65	0.14	4.50	4.74	19.66
0.47	1.36E+06	29.46	17.46	12.00	4.21	3.05	1.16	0.95	0.20	6.59	5.45	22.61
0.51	1.70E+06	36.79	21.80	14.99	5.26	3.89	1.37	1.12	0.24	7.78	5.16	21.40
0.54	2.09E+06	45.25	26.82	18.44	6.47	4.82	1.65	1.42	0.23	9.82	5.29	21.95
0.59	2.73E+06	58.95	34.93	24.02	8.42	6.04	2.39	2.07	0.31	14.35	5.94	24.62
0.63	3.27E+06	70.71	41.90	28.81	10.10	7.04	3.06	2.66	0.40	18.39	6.34	26.31
0.67	3.88E+06	83.94	49.74	34.20	11.99	8.43	3.57	3.10	0.47	21.43	6.23	25.83
0.69	4.25E+06	91.96	54.50	37.47	13.14	8.94	4.20	3.54	0.66	24.52	6.50	26.97
0.72	4.96E+06	107.26	63.56	43.70	15.33	10.40	4.93	4.39	0.54	30.36	6.90	28.63
0.76	5.74E+06	124.17	73.58	50.59	17.74	12.04	5.70	5.22	0.48	36.10	7.09	29.41
0.79	6.60E+06	142.77	84.60	58.16	20.40	12.99	7.41	6.48	0.93	44.81	7.66	31.75
0.83	7.55E+06	163.13	96.67	66.46	23.31	12.75	10.56	9.23	1.33	63.86	9.55	39.60
0.87	8.57E+06	185.35	109.84	75.51	26.48	15.87	10.61	9.82	0.79	67.95	8.94	37.08
0.90	9.69E+06	209.50	124.15	85.35	29.93	18.93	11.00	10.19	0.82	70.48	8.21	34.03
0.94	1.09E+07	235.32	139.45	95.87	33.62	20.58	13.04	11.90	1.14	82.33	8.53	35.39
0.98	1.22E+07	264.25	156.59	107.66	37.75	22.63	15.12	13.80	1.32	95.48	8.81	36.55
1.01	1.36E+07	294.33	174.42	119.91	42.05	26.23	15.83	14.65	1.18	101.35	8.40	34.83
1.05	1.51E+07	327.00	193.78	133.22	46.72	28.99	17.73	16.55	1.19	114.47	8.54	35.41
1.08	1.67E+07	362.01	214.53	147.49	51.72	34.02	17.70	16.52	1.19	114.27	7.70	31.93
1.12	1.85E+07	399.43	236.70	162.73	57.07	37.13	19.94	17.44	2.51	120.65	7.37	30.56
1.16	2.03E+07	439.35	260.35	178.99	62.77	44.06	18.72	16.37	2.35	113.23	6.29	26.07
1.19	2.23E+07	481.84	285.53	196.30	68.84	40.95	27.89	21.66	6.22	149.89	7.59	31.47
1.23	2.44E+07	526.98	312.29	214.70	75.29	44.35	30.94	24.04	6.91	166.31	7.70	31.92
1.26	2.66E+07	574.86	340.66	234.20	82.13	49.43	32.70	25.40	7.30	175.76	7.46	30.93
1.30	2.89E+07	625.56	370.70	254.86	89.38	45.04	44.33	38.76	5.57	268.20	10.46	43.37
1.34	3.14E+07	679.15	402.46	276.69	97.03	49.17	47.86	41.85	6.01	289.55	10.40	43.13
1.37	3.40E+07	735.72	435.98	299.74	105.12	55.40	49.71	43.47	6.24	300.73	9.97	41.35
1.41	3.68E+07	795.34	471.31	324.03	113.63	59.73	53.90	47.13	6.77	326.09	10.00	41.48
1.45	3.97E+07	858.10	508.51	349.60	122.60	66.16	56.44	49.35	7.09	341.43	9.70	40.25

8.6. Power density of different energy sources

Comparison between different energy sources is a difficult task to be carried out due to a variety of reasons, such as availability of the energy source, cost, geography of the territory, technology, storage & transportation of materials, basic infrastructure facilities, and quality of energy source, renewability, politics, environmental impacts, and long-term sustainability. Therefore, until and unless a long-term sustainable energy system is invented and implemented worldwide, an evaluation based on power density remains the only possible means to assess various power sources and to grade them.

For every energy source, power density refers to the amount of power (time rate of energy transfer) per unit volume, which is usually measured in W/m^3 . First, this section introduces one major form of renewable energy harnessed from wind with examples of how power density of a green energy sources is calculated conventionally. A comparison between the conventional wind power density and energy harnessed by VIVACE with PTC is presented proving the superiority of ocean energy conversion over wind power generation. A further comparison between VIVACE and other leading ocean converters is made by Kamal (2007) and it is briefly summarized in the following section. Energy harnessed by VIVACE is also compared with other major forms of ocean energy conversion, viz., the commercial marine turbines.

8.6.1. Wind power density

In order to compare the power density of wind to that of VIVACE, we need to find out the water flow speed corresponding to the wind flow speed. As the water to air density ratio is 830, we have

$$U_{water} = \sqrt[3]{\frac{U_{wind}^3}{830}} \quad (8.16)$$

in which U_{water} is the water flow speed corresponding to U_{wind} and 830 is the ratio of water density and air density.

According to the American Wind Energy Association, wind power density (WPD) is measured in watts per square meter, which indicates the amount of energy that is avail-

able at the site of energy conversion by a wind turbine.

Currently, Roscoe Wind Farm (RWF) is the world's largest onshore wind farm in the world. It is situated 45 miles southwestern of Abilene in Texas, USA and it is owned, and operated by Germany-based E.ON Climate and Renewables (EC&R). With an installed capacity of 781.5MW, the RWF exceeds the capacity of the previous largest Horse Hollow Wind Energy Center (735.5MW) in the world located in Taylor and Nolan counties southwest of Abilene. The plant is situated in 100,000 acres ($4.046 \times 10^8 \text{ m}^2$) of land and it has been operational since October 2009. The wind farm employs 627 turbines supplied by Mitsubishi, Siemens AG and General Electric. The turbines installed at the farm range between 350ft and 415ft tall, and stand 900ft apart. Out of the total number of turbines employed, 209 were the Mitsubishi 1000A model with a rated output of 1.0MW.

The rated wind speed for the wind turbines in Roscoe wind farm is 13 m/s. For a wind availability of 30%, the actual wind power output is $781.5 \times 0.30 = 234.65\text{MW}$. For a total height of the wind turbine of 415ft (126m), the occupied volume is $404.6\text{km}^3 \times 0.126\text{m} = 50.97\text{km}^3$. Therefore, the power density of the Roscoe wind turbine is:

$$\begin{aligned}\text{Power Density (Wind turbine @ 13 m/s)} &= 236.65 \text{ MW}/50.97 \text{ km}^3 \\ &= 4.64 \text{ MW}/\text{km}^3\end{aligned}$$

In addition, Lee (2009) has calculated the power density for the formerly largest wind farm, Horse Hollow Wind Energy Center, as $10.1 \text{ MW}/\text{km}^3$. It can be seen that although the recently implemented Roscoe wind farm has a larger capacity than the Horse Hollow Wind Energy Center, when assessing the level of power density, wind turbines from Horse Hollow outperform the ones at Roscoe.

Based on the experimental results from Section 8.5. To compare the power density between wind turbine farms and VIVACE, several factors should be considered:

1. Corresponding water flow speed: To have a fair comparison, we need to find the water flow speed corresponding to the rated wind speed of 13 m/s. Let us recall the equation (8.16), the corresponding water flow speed is:

$$U_{\text{water}} = \sqrt[3]{\frac{(13\text{m/s})^3}{830}} = 1.38 \text{ m/s}$$

2. Wind turbines occupy land space and have a considerable height – about 100m. That three-dimensional space is definitely valuable and should be included in the denominator. VIVACE is designed as a three dimensional device as well that can harness energy from the complete volume it occupies and the power density of VIVACE presented in Table 12. Let us also consider the efficiency of generator used for energy harnessing. According to the RETScreen (Clean Energy Project Analysis Software), a value of 95% represents the efficiency of most generators used for a small hydro clean energy plant. This value should be reduced to 93% for plants that require a gearbox. For VIVACE, a gearbox is required for converting the linear motion to rotation, therefore a 93% of efficiency is used. Availability of water flow (including maintenance down-time) of 80% was assumed. From Table 12, the power density of VIVACE at flow speed 1.37 is 300.73 w/m³. Considering the efficiency of generator and lose from transmission, the power density of VIVACE is:

$$\begin{aligned} \text{Power Density (VIVACE @ 1.37 m/s)} &= 300.73 \text{ W/m}^3 * 80\% * 93\% \\ &= 223.74 \text{ W/m}^3 \\ &= 223,743 \text{ MW/km}^3 \end{aligned}$$

The ratio of power density of RWF and that of VIVACE converter is

It is clearly that VIVACE outperforms the wind plants when assessing the power density level of each. This comparison gives us an achievable target for future development.

8.6.2. Comparison of VIVACE and other current turbines

The design of VIVACE allows flexibility in terms of scales—it can be modified based on the size of modules used to build the device. For instance, a VIVACE device can be manufactured and installed to generate electricity with a cylinder diameter of 5cm and length of 40-60cm to thousands of modules with cylinders of 1m in diameter and

20m in length. Due to this modular feature, VIVACE can be designed in different ways to generate electricity from ocean/river currents in a variety of configurations.

With the flexibility in the VIVACE Converter design, Karmal (2007) calculated basic design variables for building a VIVACE farm under a given power output, by limiting the number of cylinders to decrease complexity in mathematical calculation. He further compares the VIVACE operation with three other leading wave energy converters, Pelamis, OPY Power buoy, and the Energetech converters. Two benchmarking comparable scales were generated: a small scale with 100kWatt device, and a mega scale with 7.6kWatt. In Kamal's (2007) energy density assessment between these two VIVACE configurations (small- and mega-scale), and three other leading converters (Pelamis, PowerBouy, and Energetech's OWC), VIVACE in both configurations (small and mega scale) consistently provide a higher power density level. Specifically, the small scale VIVACE has an advantage over other devices when the device weight is included in the assessment criteria. On the other hand, the mega-scale VIVACE outperforms all devices when footprint volume blocked by the device is taken into account and it also has overall the greatest power volume density overall. In summary, Karmal (2007) successfully proves that VIVACE presents the most satisfactory and promising performance results among the leading hydrodynamic power harness devices.

Karmal (2007) provides that VIVACE allows alterations in design, and this feature of flexibility has made a major contribution of this dissertation—as the introduction of PTC is one technique to change the location of the dead zones on the Reynolds number scale, potentially allowing the VIVACE device to adjust to unknown flow conditions in an effective manner. More specially, in section 8.2, it is proved that VIVACE with PTC is more efficient than VIVACE with smooth cylinders.

This section aims to further compare features and functions of this modified VIVACE with a developing area of marine engineering—marine tidal turbines. The mechanism of marine turbines is highly sensitive to tidal resources, specifically the velocity. Unfortunately, although tidal stream resource is essentially enormous, flow velocities in most sea areas are too low to deploy technology. Therefore, the sitting requirements for

marine turbines are very specialized, a “pinch point” with peak velocities exceeding about 2-3m/s is required for a cost-effective energy recovery (Fraenkel, 2005). The risks and costs to develop marine renewable energies are in fact much higher than the land-based options, leading to limited prior research and development of large-scale deployment of marine turbines.

Data from two of the UK-based, world’s leading tidal energy companies will be used to compare with VIVACE with PTC: (1) Marine Current Turbines (MCT) Ltd., which owns the Seaflow and SeaGen projects, accredited as a UK power station with Renewable Obligation Certificates, and (2) Atlantis Resources Corporation, which owns by far the world’s largest marine turbine AK-1000 implemented in August 2010 in Scotland.

The basic performance of a marine current turbine can be modeled by using the blade element momentum theory (BEM), which suggests that the performance of a rotor is related to the match of the blade forces with to the momentum changes occurring in the fluid flowing through the rotor disc between the radii (Batten, 2006). For marine turbines, with the blade designed based on BEM, the level of energy generated is affected by density of water, the sweep area of the turbine, flow velocity, and turbine efficiency. The energy level of marine turbines can be calculated from:

$$P_{\text{harm}} = \frac{1}{2} \xi \rho A U^3 \quad (8.17)$$

where η is turbine efficiency, P_{harm} is power generated by turbine, A is the sweep area of the turbine (m^2), and U is current velocity. Features and technical structures of the three marine turbines, Seaflow, Seagen, and AK-1000 are presented in the following sections to be compared with device efficiency of VIVACE with PTC.

Turbine efficiency of these three projects is comparable with VIVACE because current VIVACE device efficiency can be calculated considering the multiple cylinder arrangements and configurations. On the other hand, the data obtained from Seaflow, Seagen and AK-1000 is based upon a single marine turbine, mainly focusing on one rotor’s efficiency for each project. If the marine turbine companies decide to arrange multiple turbines in a power plant, turbine efficiency will only decrease due to the interruption in-

produced by arranging multiple devices in the same flow system. Currently, every rotor of the marine turbines has been carefully designed based on the blade momentum theory, and each project only involves a single turbine. In addition, the configuration of VIVACE takes the distance between each cylinder into account. In other words, we are comparing VIVACE with other marine turbines with comparative advantages given to these commercial products.

Marine Current Turbine’s 300kW “Seaflow” Project:



Figure 8.21. Seaflow The 11 m diameter rotor shown raised for maintenance on left and lowered for power operation on right (Fraenkel, 2007).

Figure 8.21 shows the patented feature of the 300kW Seaflow project owned by the Marine Current Turbine (MCT) Company, which was installed in May 2003 in Southwest England. The Seaflow turbine has a single 11m-diameter rotor, with a full span pitch control. Served as a pilot project to test technical feasibility of marine turbines, the Seaflow was installed in a mean depth of seawater of 25m approximately 1.1km off the nearest landfall. The structure is supported on a tubular steel monopile with 2.1m outside diameter and 52m long. The power train is submersible.

Figure 8.22 presents the typical power harnessed from the Seaflow turbine under var-

various flow speeds at hub height for two test runs: one at neaps (light grey points) and one at springs (dark grey points). Curves for three power coefficients (C_p) are generated and presented as below.

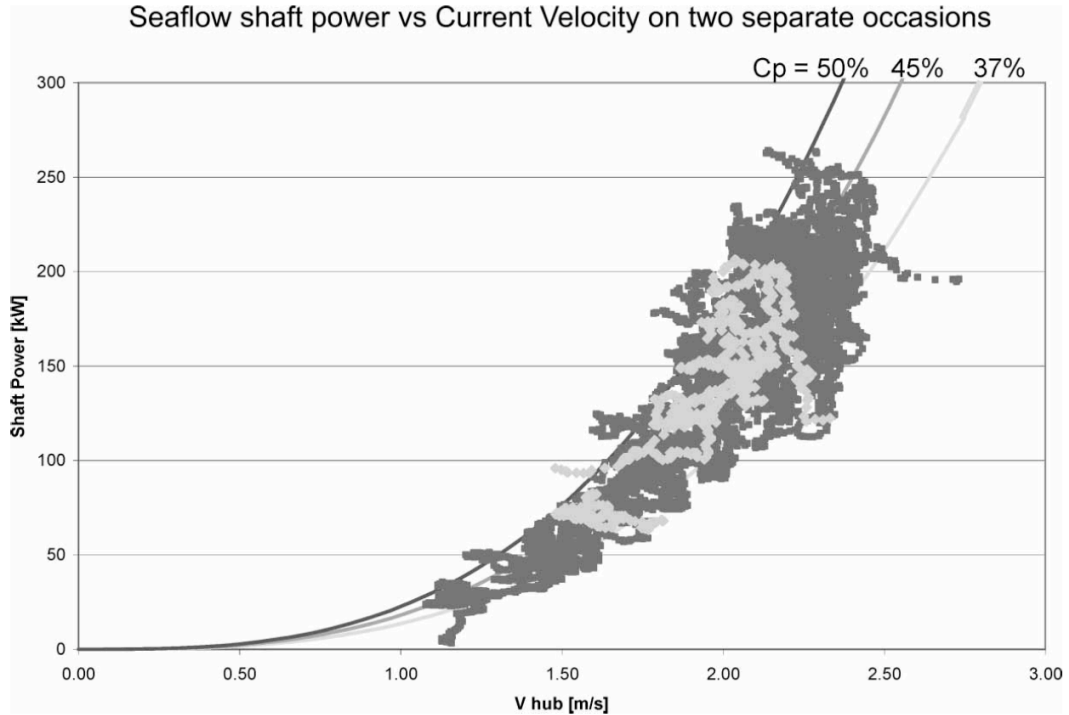


Figure 8.22. Seaflow shaft power vs. current velocity on two separate occasions (Fraenkel, 2007).

From Figure 8.22, it can be observed that when the Seaflow harnesses the greatest power level at 300kW, the average flow speed is approximately 2.5 m/s at most. This velocity (2.5 m/s) is thus used as a benchmark to calculate Seaflow’s turbine efficiency. By substituting known factors into the equation presented in Section 8.5.3, the turbine efficiency for MCT’s 300kW Seaflow project is $\eta_{\text{Seaflow}} = 0.39$ (39%), under a flow speed of 2.5 m/s.

Marine Current Turbine’s 1MW “Seagen” Project:

The Seaflow presented in the last section appears to be a feasibility test for marine turbines’ technical functions from the Marine Current Turbines Ltd. The MCT further built a commercial prototype, the Seagen, to prove marine turbine’s economic and commercial

feasibility. Seagen inherited most of the features from Seaflow. It still has a submersible power-train, a full-span pitch control with carbon/glass fiber composite rotor blades. The main support structure is the same rolled-steel monopile, except it is 3m in diameter for the Seagen, while it is 2.1m in diameter for the Seaflow. The major difference between these two projects is that the successor Seagen project has a ‘cross-arm’ feature, aiming to carry power trains from both sides, as shown in Figure 8.23.

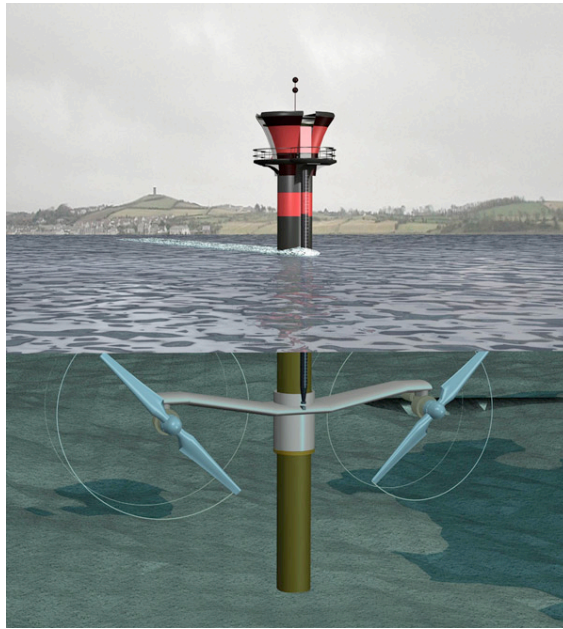


Figure 8.23. Artist’s impression of Seagen 1MW tidal turbine

To assess turbine efficiency for the Seagen, it is necessary to identify its rotor features and performance. The Seagen system has wing-like arms with 16m diameter in each rotor, allowing bi-directional operations with the rotors clear off the pile wake when they are situated downstream of the pile. The MTC reports that this tidal turbine generates a 600kW power-train per rotor with a total of 1200kW energy harnessed. Assuming that the Seagen is placed in a location with the same benchmarking flow speed as the Seaflow (2.5 m/s), the turbine efficiency calculated for each single ‘wing’ is $\eta_{\text{Seagen}} = 0.37$ (37%).

Atlantis Resource Corporation: AK1000:

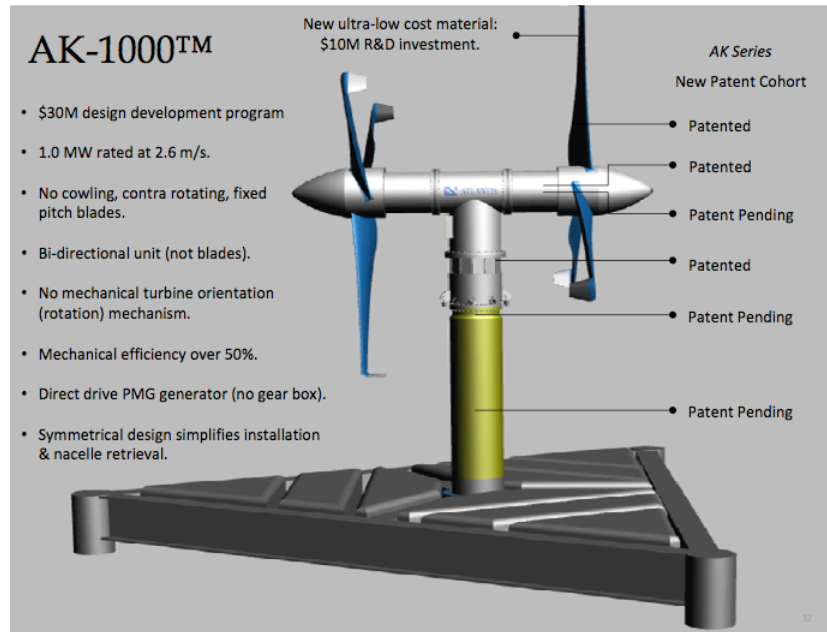


Figure 8.24. AK-1000 Artistic Impression (Atlantis Resource Corporation, 2009).

Another UK-based marine engineering firm, the Atlantis Resource Corporation, designed this by far the world's largest commercial scale Horizontal Axis Turbine, the AK-1000 (Figure 8.24), for an open ocean deployment. Unlike the Seaflow and Seagen patented by the Marine Current Turbine Ltd., the AK-1000 features a twin rotor set with fixed pitch blades. Each rotor diameter of it is 18m. The device does not require a sub-sea nacelle rotation, aiming to improve its reliability.

The first AK-1000 was deployed in August 2010 in Scotland, which stands 22.5m tall and weighs 1,300 tones. It can generate 1MW providing enough electricity for about 1,000 homes. The rated flow velocity for AK-1000 is 2.65 m/s, which suggests that this device is capable of standing a harsh environment with rough water tides.

Using the same equation used to calculate turbine efficiency, the efficiency of AK-1000 is 41%, under flow speed of 2.65 m/s.

VIVACE with PTC:

The device efficiency of VIVACE with PTC has been calculated and presented in Table 12, $P_{\text{ham}}/P_{\text{channelDL}}$. Due to the hardware limitation of the LTFSW as mentioned earlier in the dissertation, the maximum operating flow speed for is 1.45 m/s. We use the power density value obtained at maximum velocity presented in Table 12 (instead of using a value calculated by curve-fitted power density equation 8.8.) to compare with the efficiency of the three commercialized marine turbines. Table 13 presents a comparison of device efficiency of VIVACE and the three marine turbines.

TABLE 13. EFFICIENCY OF OCEAN ENERGY CONVERTERS

Device	Velocity (m/s)	Efficiency
Seaflow	2.5	39%
Seagen	2.5	37%
AK-1000	2.65	41%
VIVACE (PTC)	1.45	40.25%

It is significant to note that although current VIVACE operates in a system with the limitation of maximum flow speed of 1.45 m/s, this physical limitation does not prevent power harnessed by VIVACE with PTC from increasing even more. From Figure 8.18, for instance, the curve for power generated continues to show an upward trend at higher flow speed. Therefore, it is logical to infer that at higher flow speed, VIVACE with PTC will have better efficiency than $\eta_{\text{VIVACE}}=0.4025$ (40.25%) which is achieved at a flow speed of 1.45 m/s (Table 12).

In summary, after introducing Passive Turbulence to the VIVACE converter, its efficiency is increased significantly as presented in section 8.2. It not only generates satisfactory levels of energy compared to other conventional, alternative energy sources but it also outperforms many leading hydrodynamic energy converters today.

CHAPTER 9

MATHEMATICAL MODEL OF VIV

9.1. Background

To understand better the flow mechanism, a mathematical model of the system dynamics and fluid force from VIV is presented in this chapter.

9.2. Equation of motion

Let us consider Figure 9.1, which is a simple and idealized description of a spring-damper-mass one degree of freedom system, where the body is a cylinder. Following forces are acting on the cylinder:

- a) Spring force ($-K_{\text{spring}}y$): K_{spring} is the total spring constant (stiffness) from both springs, and y is the displacement in the direction which is perpendicular to the flow and cylinder axis.
- b) Damping force ($-c_{\text{system}}\dot{y}$): c_{system} is the total viscous damping coefficient of the system.
- c) External force on the cylinder ($F_{\text{fluid}}\hat{y}$): F_{fluid} is the force exerted on the cylinder by the fluid, \hat{y} is the unit normal vector in the direction of y . Product of F_{fluid} and \hat{y} give us the sum of the fluid force acting on the cylinder in the y -direction.

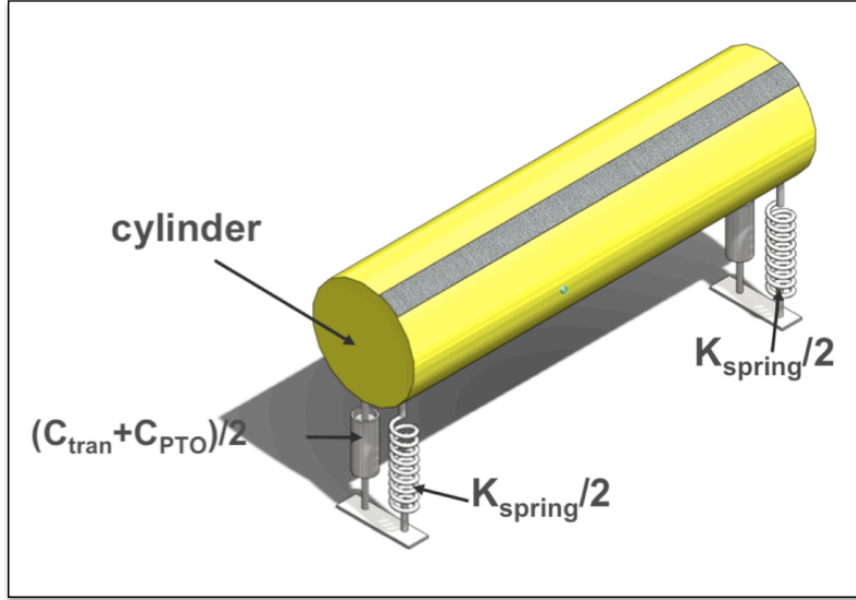


Figure 9.1. A simple schematic of circular cylinder under VIV

The second order differential equation of motion of the structure with oscillating mass m_{osc} is as follows:

$$m_{osc}\ddot{y} + c_{system}\dot{y} + K_{spring}y = F_{fluid}\hat{y} \quad (9.1)$$

Here, we separate the fluid force into viscous and inviscid components as follows

$$m_{osc}\ddot{y} + c_{system}\dot{y} + K_{spring}y = F_{viscous}\hat{y} + F_{inviscid}\hat{y} \quad (9.2)$$

The inviscid force is defined in terms of the inviscid added mass, m_a . The added mass inclusion through a constant added coefficient C_a and the added mass is defined as “the impulse given to the fluid during an incremental change of body velocity, divided by that incremental velocity.” m_a is defined as $m_a = C_a \cdot m_d$ where m_d , the mass of the displaced fluid, is $\frac{\pi}{4}\rho_{water}D^2$ per unit length for a circular cylinder. Further,

$$F_{inviscid}\hat{y} = -m_a\ddot{y} \quad (9.3)$$

$$F_{viscous}\hat{y} = -\frac{1}{2}c_y(t)\rho U^2 D \quad (9.4)$$

where c_y is the force coefficient in the y-direction, ρ is water density, U is incident flow

velocity, D is the cylinder diameter. This reduces the equation of motion to

$$(m_{osc} + m_a)\ddot{y} + c_{system}\dot{y} + K_{spring}y = \frac{2}{\pi D}c_y(t)m_dU^2 \quad (9.5)$$

We can normalize the above equation by introducing the dimensionless variables defined in the Nomenclature.

In this model, use of the natural frequency in water rather than in vacuum or air is necessary due to the big difference in density of air and water. After substituting the non-dimensional values into equation (9.5), the equation of motion becomes

$$(m^* + c_a) \cdot \left(\frac{\ddot{y}^*}{f_{n,water}^2} + \frac{4\pi\xi_{system}\dot{y}^*}{f_{n,water}} + 4\pi^2y^* \right) = \frac{2}{\pi}c_yU^{*2} \quad (9.6)$$

When the system is in resonance, the cylinder dynamics is nearly sinusoidal and VIV can be modeled using a linear oscillator model. Outside of the resonance range, the model has to be described by a nonlinear model, and several wake-oscillator models have been proposed in the literature (Blevins 1990). To obtain a simple approximation to the resonant response without experiments, the traditional approach is to assume a sinusoidal form for the fluctuating transverse force coefficient and amplitude (Bearman 1984) as

$$y^* = y^*_{max} \sin(2\pi f_{fluid}t) \quad (9.7)$$

$$c_y(t) = C_y \sin(2\pi f_{fluid}t + \phi) \quad (9.8)$$

where f_{fluid} is the dominant fluid forcing frequency which relates to the cylinder in VIV frequency. For the ensuing analysis, f_{fluid} is assumed equal to f_{osc} , which is the dominant fluid forcing frequency. Matching of these two quantities defines resonance. Further, ϕ is the phase difference between the fluid forcing and the displacement. That is, the displacement lags the forcing by an angle ϕ , which is near $\frac{\pi}{2}$ for linear system resonance.

Note that the phase angle ϕ between the fluid force and the body displacement is important in determining the energy transfer from the fluid to VIVACE. From equations (9.7) and (9.8) we can deduce that $C_y \sin\phi$ must be positive for VIVACE converter to gen-

erate energy.

9.3. Expressions for power in fluid

Next, we derive expressions for the various stages of available power and for the VIVACE energy density.

In the present analysis the power in the flowing fluid is taken over the projected area of the cylinder in the direction perpendicular to the flow direction and can be calculated as follows. The kinetic pressure head in the fluid from Bernoulli's equation is $\frac{1}{2}\rho U^2$. The force acting over the projected area DL of the cylinder in direction-x of the flow is $\frac{1}{2}\rho U^2 DL$. For an oscillating cylinder, the projected area where the cylinder encounters the fluid is $(2A+D)*L$ but this area would not be completely representative of fluid power utilized because the fluid in this projected area doesn't encounter the oscillating cylinder for the whole oscillating period, but it is the DL projected area that always encounters the flowing fluid by the cylinder. In the case of multiple cylinders, the cylinders downstream encounter unaffected fluid due to the staggered arrangement. Since there is no clear way of defining how much power from the fluid is utilized by the oscillating cylinder and for simplicity the projected area used is DL . Then, the power in the fluid, being the product of the acting force times the velocity in that same direction-x is

$$\text{Power in fluid } (P_{\text{fluid}}) = \frac{1}{2} \rho_{\text{water}} U^3 DL \quad (9.9)$$

Equation (3.9) provides a fluid power for reference. It is not appropriate to use it in the denominator in energy density calculations.

9.4. Expressions for fluid power in VIVACE

A more appropriate measure of efficiency is the one used by the Department of Energy for ocean energy converters, where energy density is measured in kW/m^3 . The implication of using energy density instead of efficiency is that it takes into consideration

the entire space affected by the converter. For example, a ducted turbine like the Lunar Power needs a downstream clearance of about 10 duct lengths and a vertical clearance of about one duct diameter (Bedard and Previsic 2005; Bedard et al. 2005). Further, moored wave energy converters obstruct use of the entire footprint volume.

The work done by the fluid force acting on a VIVACE cylinder during a vibration cycle is obtained from the inner vector product of the force by the displacement vector integrated over one cycle. Therefore, the work done on the body during a cycle of oscillation of the cylinder is

$$W_{VIVACE-Fluid} = \int_0^{T_{osc}} F_{fluid} \dot{y} dt \quad (9.10)$$

Then, the fluid power in VIVACE is

$$P_{VIVACE-Fluid} = \frac{W_{VIVACE-Fluid}}{T_{osc}} \quad (9.11)$$

The force exerted on the VIVACE cylinder by the fluid is given by the right hand side of equation (9.5). If we multiply the force by the instantaneous velocity, integrate the right hand side and average it over the cycle period T_{osc} we have:

$$P_{VIVACE-Fluid} = \frac{1}{T_{osc}} \int_0^{T_{osc}} \frac{2}{\pi D} c_y(t) m_d U^2 2\pi f_{fluid} y_{max} \cos(2\pi f_{fluid} t) dt \quad (9.12)$$

In synchronization, we have $f_{fluid} = f_{osc} = \frac{1}{T_{osc}}$. Therefore,

$$\begin{aligned} P_{VIVACE-Fluid} &= f_{osc} \int_0^{\frac{1}{f_{osc}}} \frac{2}{\pi D} c_y(t) m_d U^2 2\pi f_{osc} y_{max} \sin(2\pi f_{osc} t + \phi) \cos(2\pi f_{osc} t) dt \\ &= \frac{2}{D} C_y m_d U^2 2\pi f_{osc}^2 y_{max} \left(\frac{1}{f_{osc}} \sin(\phi) + \cos(4\pi f_{osc} + \phi) - \cos(\phi) \right) \\ &= \frac{2}{D} C_y m_d U^2 2\pi f_{osc} y_{max} \sin(\phi) \end{aligned} \quad (9.13)$$

Inserting the definition of displacement mass, $m_d = \frac{\pi}{4\pi} \rho D^2 L$, we obtain

$$P_{VIVACE-Fluid} = \frac{1}{2} \rho \pi C_y U^2 f_{osc} y_{max} DL \sin(\phi) \quad (9.14)$$

9.5. Expressions for mechanical power in VIVACE

From equation (9.5), we integrate the left hand side of the equation after multiplying it by the instantaneous velocity and we average it over the cycle period T_{osc} to obtain the mechanical power in VIVACE as

$$P_{VIVACE-mech} = \frac{1}{T_{osc}} \int_0^{T_{osc}} \left((m_{osc} + m_a) \ddot{y} + c_{system} \dot{y} + K_{spring} y \right) \dot{y} dt \quad (9.15)$$

Since we assume the amplitude response (y) is approximately sinusoidal curve. The only term in phase with the velocity (\dot{y}) generates a non-zero term. Thus,

$$\begin{aligned} P_{VIVACE-mech} &= \frac{1}{T_{osc}} \int_0^{T_{osc}} 4\pi(m_{osc} + m_a) \xi_{system} \dot{y}^2 dt \\ &= 8\pi^3 (m_{osc} + m_a) \xi_{system} (y_{max} f_{osc})^2 f_{n,water} \end{aligned} \quad (9.16)$$

9.6. Expression for upper limit of power in VIVACE

The actual energy harnessed of the VIVACE Converter, can be calculated based only on the harnessed energy measured during lab tests of the VIVACE model in the LTFSW Channel. Nevertheless, an upper limit can be calculated as the power in VIVACE – either in fluid form, equation (9.14) or in mechanical form, equation (9.16).

The upper limit of harnessed power on VIVACE can be defined as

$$P_{UL-VIVACE} = \frac{1}{2} \rho \pi C_y U^2 f_{cyl} y_{max} DL \sin(\phi) \quad (9.17)$$

For any given experiment, if U , D , L , ρ , m^* are fixed; f_{osc} , y_{max} and Φ are measured; C_y is calculated as follows:

In equation (9.7), for $t = \frac{1}{4} T_{osc}$ and $\frac{3}{4} T_{osc}$, the displacement is at its maximum, veloc-

ity is zero, thus eliminating the term with the unknown damping and acceleration is at its maximum. So,

$$y(t = \frac{1}{4}T_{osc}) = y_{max} \sin(2\pi f_{fluid} \frac{1}{4}T_{osc}) = y_{max} \quad (9.18)$$

$$\ddot{y}(t = \frac{1}{4}T_{osc}) = -\omega^2 y_{max} \sin(2\pi f_{fluid} \frac{1}{4}T_{osc}) = -\omega_{osc}^2 y_{max} \quad (9.19)$$

Using the potential value of m_a for inviscid flow and equations (9.5), (9.7) and (9.8), we drive the following expression from which C_y can be calculated

$$-(m_{osc} + m_a)\omega_{osc}^2 y_{max} + 0 + K_{spring} y_{max} = \frac{1}{2} \rho C_y U^2 DL \sin(\frac{\pi}{2} + \phi) \quad (9.20)$$

And the value of upper limit power of VIVACE can be obtained from equation (9.17). However, Φ is not measured in the experiments in this dissertation. Another method is applied to calculate the theoretical upper limit of harnessed power on VIVACE in the LTFSW Channel. According to Betz (Cuevas et al. 2006), this limit can be calculated for the flow in the LTFSW Channel as follows.

Let U_{up} and U_{down} be the flow velocity measured from upstream and downstream side of the VIVACE apparatus, respectively. The mean flow velocity can be expressed as

$$\bar{U} = \frac{U_{up} + U_{down}}{2} \quad (9.21)$$

The mass flow rate through the cross section area of channel is:

$$\begin{aligned} \dot{m}_{flow} &= \rho W_{channel} \times D_{channel} \times \bar{U} \\ &= \rho W_{channel} \times D_{channel} \times \left(\frac{U_{up} + U_{down}}{2} \right) \end{aligned} \quad (9.22)$$

where $W_{channel}$ is the width of water channel and $D_{channel}$ is the depth of water channel. The converted power from the flow is the difference between hydrokinetic energies upstream and downstream of VIVACE. Here, we assumed that velocity measured on upstream equals to incident flow velocity ($U_{up}=U$) and it yields:

$$\frac{1}{2}\dot{m}_{flow}U_{up}^2 - \frac{1}{2}\dot{m}_{flow}U_{down}^2 = \frac{\rho}{2}W_{channel}D_{channel}U^3\left(1 + \frac{U_{down}}{U}\right)\left[1 - \left(\frac{U_{down}}{U}\right)^2\right] \quad (9.23)$$

From equation (9.23), the upper limit harnessed power (maximum harnessed power) occurs when $\frac{U_{down}}{U} = \frac{1}{3}$. The theoretical upper limit of harnessed power is :

$$P_{UL-VIVACE} = \frac{16}{27}\frac{\rho}{2}W_{channel}U^3 \quad (9.24)$$

9.7. Expression for harnessable energy using VIVACE

The power that we can harness using the VIVACE Converter is the power extracted by the generator which is equal to the power VIVACE extracts from the fluid minus the power dissipated by structural, transmission, and internal generator losses. To simplify calculations, we assume that the damping force due to the generator, which converts the mechanical energy to electrical energy, is in phase with the velocity term and it behaves in the same way as structural and transmission damping. The total damping of VIVACE used in this dissertation is defined as $c_{system} = c_{structure} + c_{harn}$, in dimensionless form

$$\zeta_{system} = \zeta_{structure} + \zeta_{harn} \quad (9.25)$$

Ideally, if we take off the $\zeta_{structure}$, which is considered as dissipated power in the system from ζ_{total} , the remaining damping represents the energy we can harness from fluid. From equation (9.16) and (9.25), we obtain harnessable power on VIVACE as follow:

$$P_{VIVACE-mech} = 8\pi^3(m_{osc} + m_a)(\zeta_{system} - \zeta_{structure})(y_{max}f_{osc})^2 f_{n,water} \quad (9.26)$$

Note that ζ_{system} can be either calculated by using equation (9.19) and (9.20) or estimate by conducting system damping identification experiment.

CHAPTER 10

MATHEMATICAL MODEL OF GALLOPING AND GALLOPING INSTABILITY

10.1. Background

In this section, an attempt is made to model galloping instability observed in present study for rough cylinders (with PTC). When a bluff body is exposed to a uniform flow, the flow separates from either sides of the body, leading to a broad wake encompassed within two free shear layers. These layers curl and form vortices in the wake generating alternating pressure fluctuations on the surface of the body, thereby induce periodic forces and oscillations. For right circular cylinders, this is the mechanism underlying their flow-induced motions commonly referred as ‘Vortex-Induced Vibrations’ (VIV). But, for a non-circular section such as the one used in present study, when the cylinder is slightly displaced from its equilibrium position (due to oscillation), the resulting flow structures on either side of the cylinder will become greatly asymmetric due to the continuously changing flow incidence angle. This asymmetry of flow structures in turn is caused by the angle of attack inducing additional hydrodynamic forces in the direction of body motion that leads to very large excitation amplitudes called ‘galloping instability’. Such a generation of additional hydrodynamic forces is analogous to the induction of ‘negative hydrodynamic damping’ in the system. Thus, the mechanism behind this kind of vibration is different from that of the vortex induced vibrations.

10.2. Mathematical model

The mathematical equation of motion of a simple elastically mounted cylinder is

$$(m_{osc} + m_a)\ddot{y} + 2\zeta_{system}\omega_n(m_{osc} + m_a)\dot{y} + K_{spring}y = F_{fluid}\hat{y} = F_y \quad (10.1)$$

where m_{osc} , m_a is the hydrodynamic mass per unit length, which is considered as $\frac{1}{4}\pi D^2$, ξ_s is structural damping ratio, ω_n is natural angular frequency of cylinder in water, k_{spring} is stiffness and F_y is the transverse force exerted on the cylinder in the direction of the initial displacement. Let us consider the force term in the above equation. In Figure 10.1, F_y can be expressed as

$$F_y = -F_L \cos \alpha - F_D \sin \alpha, \quad \alpha = \arctan(\dot{y}/U) \quad (10.2)$$

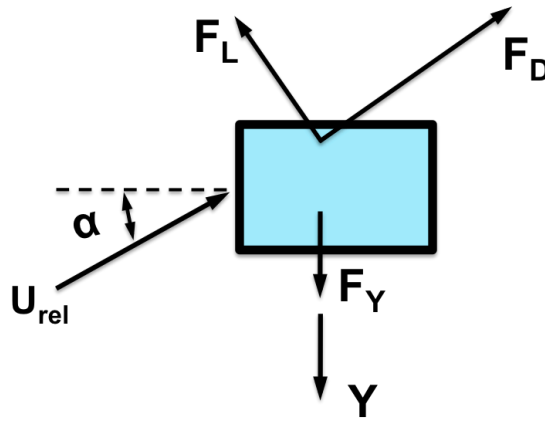


Figure 10.1. Fluid forces exerting on the rectangular cylinder

α is the so-called angle of attack. Here $\alpha=0$ has been referenced to the equilibrium position. The velocity of flow relative (U_{rel}) to the moving model is the sum of the free stream velocity (U) and the induced velocity (\dot{y}) as follow.

$$U_{rel}^2 = \dot{y}^2 + U^2 \quad (10.3)$$

F_L and F_D are also defined as

$$F_L = \frac{1}{2} \rho U^2 D C_L \quad (10.4)$$

$$F_D = \frac{1}{2} \rho U^2 D C_D \quad (10.5)$$

where C_L is lift force coefficient and C_D is drag force coefficient. From equation (10.1),

(10.2), (10.4) and (10.5), the governing equation can be re-written as

$$(m_{osc} + m_a)(\ddot{y} + 2\xi_{system}\dot{y} + \omega_n^2 y) = F_y = \frac{1}{2}\rho U^2 D C_y \quad (10.6)$$

where

$$C_y = -C_L \cos \alpha - C_D \sin \alpha \quad (10.7)$$

For a small angle of attack (α), the coefficient C_y is hydrodynamic force coefficient. For small angle of attack, $\alpha \sim 0$, the coefficient C_y

$$C_y \approx C_y(\alpha = 0) + \alpha \left(\frac{\partial C_y}{\partial \alpha} \right)_{\alpha=0} \quad (10.8)$$

$C_y(\alpha=0)$ is found from Equation (10.7) as

$$C_y(\alpha = 0) = -C_L(\alpha = 0) \equiv 0 \quad (10.9)$$

Also, from Equation (10.7) again, $\left(\frac{\partial C_y}{\partial \alpha} \right)_{\alpha=0}$ can be obtained

$$\left(\frac{\partial C_y}{\partial \alpha} \right)_{\alpha=0} = - \left(\frac{\partial C_L}{\partial \alpha} \right)_{\alpha=0} - C_D(\alpha = 0) \quad (10.10)$$

Now substituting Equation (10.9) and (10.10) into Equation (10.8) gives

$$C_y = - \left[\left(\frac{\partial C_L}{\partial \alpha} \right)_{\alpha=0} + C_D(\alpha = 0) \right] \alpha \quad (10.11)$$

Since definition of α from Equation (10.2), C_y can be rewritten as

$$C_y = - \left[\left(\frac{\partial C_L}{\partial \alpha} \right)_{\alpha=0} + C_D(\alpha = 0) \right] \frac{\dot{y}}{U} \quad (10.12)$$

and

$$F_y = \frac{1}{2} \rho D U^2 C_y = -\frac{1}{2} \rho D U \left[\left(\frac{\partial C_L}{\partial \alpha} \right)_{\alpha=0} + C_D(\alpha=0) \right] \dot{y} \quad (10.13)$$

Now, substituting equation (10.13) into equation of motion, we get

$$\ddot{y} + 2\zeta_{total} \omega_n \dot{y} + \omega_n^2 y = 0 \quad (10.14)$$

where ζ_{total} , the total damping ratio from both fluid and system, is defined as

$$\begin{aligned} \zeta_{total} &= \zeta_{system} + \frac{1}{4} \frac{\rho D U}{(m_{osc} + m_a) \omega_n} \left[\left(\frac{\partial C_L}{\partial \alpha} \right)_{\alpha=0} + C_D(\alpha=0) \right] \\ &= \zeta_{system} + \frac{1}{4} \frac{\rho D U}{(m_{osc} + m_a) \omega_n} \left(\frac{\partial C_y}{\partial \alpha} \right)_{\alpha=0} \end{aligned} \quad (10.15)$$

Solution to equation (10.14) is

$$y = \frac{\frac{1}{2} \rho U^2 D C_L(\alpha=0)}{K_{spring}} + A_y \exp(-\zeta_{total} \omega_d t) \sin(\omega_d t + \phi) \quad (10.16)$$

where ω_d is the damped angular natural frequency:

$$\omega_d = \omega_n \sqrt{1 - \zeta_{total}^2} \quad (10.17)$$

The oscillatory component can either increase with time (unstable vibrations) or decrease with time (stable vibration) depending on the sign of the net damping coefficient in the system. Vibrations will increase with time for all angle of attack for which $\zeta_{total} < 0$, which is the case if the slope of vertical force coefficient (C_y) is positive. Thus, the model will be unstable if

$$\frac{\partial C_y}{\partial \alpha} > 0 \quad \text{or equivalently,} \quad \frac{\partial C_L}{\partial \alpha} + C_D < 0 \quad (10.18)$$

and stable otherwise (Den Hartog, 1956). By setting $\zeta_{total}=0$, the critical velocity for onset of plunge galloping instability becomes

$$\frac{U_{critical}}{f_n D} = \frac{4(m_{osc} + m_a)(2\pi\zeta_{system})}{\rho D^2} / \frac{\partial C_y}{\partial \alpha} \quad (10.19)$$

Applying non-dimensional parameter reduced velocity (U^*) and M^* to Equation (10.19), it yields

$$U^*_{gallop} = \frac{4(m_{osc} + m_a)(2\pi\zeta_{structure})}{\rho D^2} / \frac{\partial C_y}{\partial \alpha} = 8\pi M^* \zeta_{system} / \frac{\partial C_y}{\partial \alpha} \quad (10.20)$$

Mass ratio per unit length, M^* is defined as

$$M^* = \frac{(m_{osc} + m_a)}{\rho D^2} \quad (10.21)$$

For the purpose of studying the relationship between body geometry and PTC location on galloping response, the vertical force coefficient is first expressed as a polynomial in \dot{y}/U , since angle of attack α is a function of this parameter:

$$C_y(\alpha) = a_0 + a_1\left(\frac{\dot{y}}{U}\right) + a_2\left(\frac{\dot{y}}{U}\right)^2 + a_3\left(\frac{\dot{y}}{U}\right)^3 + \dots \quad (10.22)$$

The first two coefficients are determined by the vertical lift force and its slope at zero angle of attack, and also the drag force coefficient (at $\alpha=0$) as shown below

$$a_0 = -C_L, \quad a_1 = \frac{\partial C_y}{\partial \alpha} = -\left(\frac{\partial C_L}{\partial \alpha}\right)_{\alpha=0} - C_D(\alpha=0) \quad (10.23)$$

The coefficients are determined by curve-fitting experimental data for $C_y(\alpha)$ over an appropriate range of α . Note that, if the section is symmetric about a line in the direction of the flow through the center of the section, only odd harmonics a_1 , a_3 , etc in the series are non-zero. The transverse force (F_y) exerting on the cylinder and critical reduced velocity for galloping can be expressed as

$$F_y = \frac{1}{2} \rho D U^2 \left[a_1 \left(\frac{\dot{y}}{U}\right) + a_3 \left(\frac{\dot{y}}{U}\right)^3 \right] \quad (10.24)$$

$$U_{gallop}^* = 8\pi M^* \zeta_{system} / a_1 \quad (10.25)$$

We substitute equation (10.24) to the governing equation of motion. Employing the Krylov-Bogoliuvov method as follows can solve the equation of motion and obtain the amplitude of oscillation as,

$$A^* = \left(\frac{2U^*}{3\pi a_3} \left(4M^* \zeta_{system} - a_1 \frac{U^*}{2\pi} \right) \right)^{1/2} \quad (10.26)$$

A^* is normalized amplitude of oscillation defined as $A^*=y/D$.

Both coefficients a_1 and a_3 demonstrate a dependence on several factors such as cross-section geometry, aspect ratio of the body, and characteristics of the incident flow. In fact, the effects of PTC location on galloping response will be further investigated based on these factors.

10.3. Effect of PTC on transverse galloping

VIVACE presented in this dissertation mainly utilizes two hydrodynamic forces, viz., VIV and galloping to get the maximum amplitude ratio. VIV of smooth circular cylinder on VIVACE has been fully investigated by Kamal (2006) and Lee (2009). The large-amplitude galloping motion is first found on a single circular cylinder with roughness strips applied on certain surface location. The geometrical parameters affecting galloping will be investigated in this section.

Galloping is a type of aero/hydrodynamic instability characterized by a large amplitude, and a low frequency motion occurring normal to the flow. As indicated earlier, galloping requires some asymmetry of the body cross-section to the relative flow during oscillation. As is well known, a smooth circular cylinder cannot gallop due to its symmetric feature (Alonso, 2009). But, a circular cylinder attached with PTC in certain location is no longer considered as symmetric; on the other hand, it is essentially a non-circular section prone to galloping instability. The principal qualitative differences between VIV and galloping are,

#1: Galloping occurs typically in a flow speed above a critical point U , and this phenomenon is dependent upon the system damping, mass ratio and the cross-section geometry of the structure. VIV oscillations occur only in a discrete range.

#2: The amplitude of galloping oscillation is usually very large and it continues to increase with a greater flow velocity until the structure possibly collapses. This is the case for classical galloping. For isolated square sections, in certain structural and flow conditions, the amplitude grows to a very large value with increasing flow velocity and remains stable without further increase even though the flow velocity keeps increasing. This is also adjudged as a class of galloping (Takeuchi, 1992). In the case of VIV, the amplitude will exhibit only a limited growth with respect to flow velocity and will diminish thereafter. This exemplifies that excitation is ‘self-limiting’. In addition, the vortex-shedding frequency during VIV will be locked-on to the oscillation frequency without showing an abrupt increase over a range of flow velocity. In the case of galloping, the vortex shedding frequency can increase with respect to flow velocity similar to that of a stationary body (Bokaian G. , 1984). Moreover, the wake patterns of galloping can be markedly different from that of VIV.

#3. VIV oscillation frequencies can go higher than natural frequency of the structure (about 1.2 times); whereas, galloping frequencies are generally lower.

The three differences presented above are critical for examining the experimental results of the present study, by providing a foundation to develop a mathematical model of galloping of circular cylinder with PTC.

Numerous studies on galloping instability indicate that the two empirical coefficients a_1 and a_3 from equation (10.24) demonstrate a strong dependence on several factors, namely the cross-section geometry, aspect ratio and the characteristics of the incident flow (Blevins 1977). Considering all these factors, the relation between a_1 , a_3 (empirical coefficients) and configuration of PTC (cross-section geometry) is further explored with inferences from the experimental results of present study as will be portrayed in the following analysis.

10.3.1. Galloping instability

The critical reduced velocity for galloping instability is a function of mass ratio (M^*), system damping (ζ_{total}), and cross-section coefficient a_1 and is given by,

$$U_{gallop}^* = 8\pi M^* \zeta_{total} / a_1$$

In all experiments conducted in this study, M^* and ζ_{total} are fixed values representing known quantities. If the critical reduced velocity can be found, the relation between a_1 and PTC configuration can be established. The definition of galloping instability on this VIV and galloping associated motion is derived from series of examination as following.

In connection with the occurrence of galloping, four possible critical reduced velocity values are identified. (A) U^* at which frequency stops to increase, U^*_a , (B) U^* at which frequency starts to drops down, U^*_b , (C) U^* at which oscillation frequency becomes nearly equals to the natural frequency, U^*_c , and (D) U^* at which the oscillation amplitude abruptly increases, U^*_d . These values are defined and listed in Table 14. By applying the values of U^*_{gallop} obtained from different configurations of PTC to equation (10.25), a_1 for each PTC configuration can be calculated. The calculated values of a_1 are presented in Tables 15, 16 and 17 and correspond to three groups of data as detailed below.

Group 1: In this group of tests, PTC roughness is fixed (P120) and applied on the cylinder surface at various locations (Table.15). In these circumstances, changes in the body geometry are attributed to different PTC locations.

Group 2: In this group of tests, PTC location is fixed at 20° to 36° while the roughness level of PTC varies (Table.16). In these cases, changes in the body geometry are attributed to levels of PTC roughness.

Group 3: In this group of tests, a PTC configuration of P60: 20° to 36° is chosen varying the spring stiffness (Table.17). Therefore, the cross-section geometry is essentially the same across all the cases in this group.

TABLE 14. DEFINITION OF EACH CHOSEN CRITICAL REDUCED VELOCITY

	Definition	Explanation
U^*_a	The reduced velocity at which the frequency of oscillation (f_{osc}) stops increasing.	U^*_a and U^*_b : One of the characteristics of galloping is “low frequency motion”. In VIV, the frequency of oscillation (f_{osc}) is proportional to flow speed in a constant value. On this point of view, we can assume that once f_{osc} stops increasing or starts dropping (contrary to the nature of VIV), there is another hydrodynamic force occurring and exerting on the cylinder. In some PTC configurations, U^*_a and U^*_b are equal.
U^*_b	The reduced velocity at which the frequency of oscillation (f_{osc}) starts dropping.	
U^*_c	The reduced velocity at which the frequency of oscillation (f_{osc}) equals to natural frequency in water ($f_{n,water}$).	Galloping occurs at oscillating frequency ratio ($f_{osc}/f_{n,water}$) at one.
U^*_d	The reduced velocity at which the oscillating amplitude shoots up.	One of the galloping characteristics is large oscillating amplitude.

TABLE 15. GROUP 1: a_1 CALCULATED FROM STUDY OF PTC LOCATION.

A				B			
Location	U^*_a	ReD	a_1 (U^*_a)	Location	U^*_b	ReD	a_1 (U^*_b)
20-36	9.7	7.89E+04	0.0586	20-36	9.7	7.89E+04	0.0586
30-46	9.08	7.33E+04	0.0627	30-46	9.08	7.33E+04	0.0627
40-56	8.03	6.48E+04	0.0708	40-56	9.7	7.89E+04	0.0586
50-66	7.8	6.20E+04	0.0729	50-66	9.7	7.89E+04	0.0586
64-80	7.5	6.00E+04	0.0759	64-80	7.5	6.00E+04	0.0575

C				D			
location	U^*_c	ReD	a_1 (U^*_c)	Location	U^*_d	ReD	a_1 (U^*_d)
20-36	13.27	1.07E+05	0.0429	20-36	11	9.00E+04	0.0517
30-46	12.9	1.04E+05	0.0441	30-46	11	9.00E+04	0.0517
40-56	12.2	9.87E+04	0.0466	40-56	10.82	8.74E+04	0.0526
50-66	11.87	9.59E+04	0.0479	50-66	11	9.00E+04	0.0517
64-80	n/a	n/a	n/a	64-80	n/a	n/a	n/a

TABLE 16. GROUP 2: a_1 CALCULATED FROM STUDY OF PTC ROUGHNESS.

A				B			
Roughness	U^*a	ReD	a_1 (U^*a)	Roughness	U^*b	ReD	a_1 (U^*b)
P150	9.7	7.89E+04	0.0586	P150	9.7	7.89E+04	0.0093
P120	9.7	7.89E+04	0.0586	P120	9.7	7.89E+04	0.0093
P80	9.7	7.89E+04	0.0586	P80	9.7	7.89E+04	0.0093
P60	9.7	7.89E+04	0.0586	P60	9.7	7.89E+04	0.0093

C				D			
Roughness	U^*c	ReD	a_1 (U^*c)	Roughness	U^*d	ReD	a_1 (U^*d)
P150	11.5	9.30E+04	0.0494	P150	11.5	9.30E+04	0.0494
P120	11.17	9.02E+04	0.0517	P120	11.17	9.02E+04	0.0517
P80	10.47	8.74E+04	0.0543	P80	10.47	8.74E+04	0.0543
P60	9.7	8.50E+04	0.0586	P60	9.7	8.50E+04	0.0586

TABLE 17. GROUP 3: a_1 CALCULATED FROM STUDY OF VARIED STIFFNESS.

K (N/m)	$\zeta_{structure, damping}$ ratio	A			B		C		D	
		ReD	U^*a	a_1 (U^*a)	U^*b	a_1 (U^*b)	U^*c	a_1 (U^*c)	U^*d	a_1 (U^*d)
400	0.0227	7.90E+04	14.5	0.0596	17.7	0.0488	18.4	0.0469	18.4	0.0469
600	0.0185	7.90E+04	12	0.0588	12.8	0.0551	14.5	0.0486	14.4	0.0490
800	0.0160	8.09E+04	10.6	0.0576	11.4	0.0536	13.1	0.0466	13.1	0.0466
1000	0.0143	7.33E+04	9.1	0.0600	9.8	0.0557	11	0.0497	11	0.0497
1200	0.0131	8.18E+04	8.7	0.0573	8.7	0.0573	9.8	0.0509	9.8	0.0509
1400	0.0121	8.18E+04	8.1	0.0570	8.1	0.0570	9	0.0513	9	0.0513
1600	0.0113	8.18E+04	7.4	0.0583	7.4	0.0583	8.25	0.0523	8.25	0.0523
1800	0.0107	7.90E+04	6.8	0.0599	6.7	0.0608	7.75	0.0525	7.75	0.0525
2000	0.0101	7.90E+04	6.5	0.0594	6.5	0.0594	7.7	0.0502	7.7	0.0502
average				0.0584	0.0562		0.0499		0.0499	
STDEV				0.0013	0.0036		0.0022		0.0021	

By inspection of the data presented in Tables 15-17 they following conclusions can be drawn. The rougher strip configuration, P60:20deg -36deg, Table 16 (Group 2) and Table 17 (Group 3) yields a consistent value for a_1 based on U^*_a , viz., $a_1 \sim 0.058$. It is also be noted that, for Group 2 (Table.16), where the PTC location is fixed, the value of a_1 is close to 0.058 irrespective of the roughness height. Specifically, when the K value is varied over a broad range, the value of a_1 is still consistent at $a_1 \sim 0.0584$. In other cases such

as (A), (B), (C) and (D), a_1 is found to be not completely consistent. $a_1=0.0584$ is derived from these distinct outcomes across different cases as a representative value for the test geometry. This confirms that the most appropriate critical reduced velocity for galloping is the point at which frequency stops to increase or starts to drop. The effect of angle of attack on the flow structures becomes noticeable at the point of frequency drop. Further, as mentioned in previous sections (refer Figure 3.2), the onset of galloping whether occurring back-to-back with VIV or independently takes place over a range of reduced velocity, and it is not a ‘single-point’ phenomenon. To recall, being initiated at the frequency dropping point, the ‘fully developed galloping’ occurs at a later reduced velocity covering a ‘transition zone’ in which the negative hydrodynamic damping becomes sufficient enough to cause a sudden amplitude increase. Furthermore, soon after the frequency dropping point, a notable increase in the slope of the response branch can be observed in almost all the cases.

For various values of surface roughness, values of ‘ a_1 ’ are calculated for different strip locations as presented in Table.18. These values are plotted in Figure 10.2. The following observations can be made:

- a) With an increase of strip placement angle, a_1 increases and critical reduced velocity (U^*_{gallop}) decreases. It is because U^*_{gallop} is inversely proportional to a_1 . It can also be noted that, a_1 registers a notable increase up to an angle of 50deg.. For a_1 from 50 to 60deg., the increase is not substantial.
- b) The coefficient a_1 is determined by the PTC location instead of the PTC roughness, meaning that the critical velocity for galloping is primarily determined by PTC location.

At a particular strip location, a_1 is almost invariant with respect to roughness height as could be seen in Figure 10.2. This corroborates well with (b).

TABLE 18. CALCULATED a_1 IN VARIED PTC ROUGHNESS AND LOCATION

	20°-36°	30°-46°	40°-56°	50°-66°	64°-80
P60	0.0586				
P80	0.0586				
P120	0.0586	0.0627	0.0708	0.0741	0.0759
P150	0.0586				

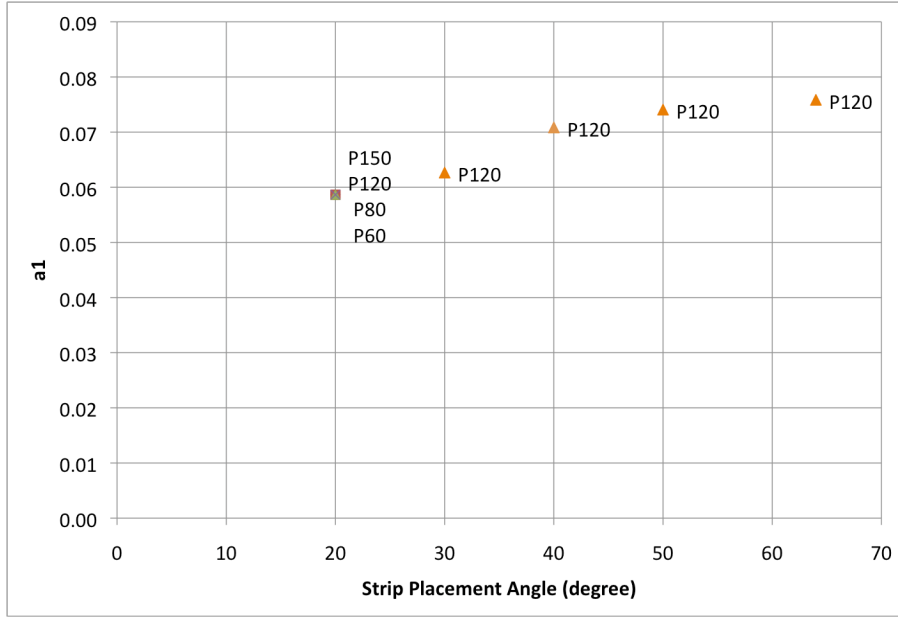


Figure 10.2. Variation of coefficient ' a_1 ' with strip placement angle and roughness

10.3.2. Estimation and analysis of geometric parameters

Let us recall equation (10.26)

$$A^* = \left(\frac{2U^*}{3\pi a_3} \left(4M^* \xi_{system} - a_1 \frac{U^*}{2\pi} \right) \right)^{1/2}$$

Differentiating the above equation yields

$$\frac{\partial A^*}{\partial U^*} = \frac{1}{2} \left(\frac{2U^*}{3\pi a_3} \left(4M^* \xi_{system} - a_1 \frac{U^*}{2\pi} \right) \right)^{-1/2} \left(\frac{8M^* \xi_{system}}{3\pi a_3} - \frac{2}{3\pi^2} \frac{a_1}{a_3} U^* \right) \quad (10.27)$$

Based on the results of amplitude response trend, the slope (LHS of equation (10.27))

can be computed. Moreover, because all other parameters are known for the system as well as for body geometry, coefficient ‘ a_3 ’ can be estimated from equation (10.28). The values of ‘ a_3 ’ are tabulated (Table 19) along with the slope ($\frac{\partial A^*}{\partial U^*}$), a_1 , U^*_{gallop} , Reynolds number at U^*_{gallop} , amplitude ratio at U^*_{gallop} and the maximum angle of attack ($\tan\Phi_{\text{max}}$). Maximum angle of attack ($\tan\Phi_{\text{max}}$) where a combined effect of VIV and galloping is expected to occur is calculated by equation (10.28).

$$\tan \phi_{\text{max}} = 2\pi \frac{(A/D)}{U^*} \quad (10.28)$$

. Therefore, the calculated values of a_3 could be susceptible to small errors, which could not be calculated herein. Hence, all the parametric values calculated based on a_3 should be considered approximate.

From Table 9 (I), it can be seen that, for a particular roughness (P120), the absolute value of coefficient ‘ a_3 ’ increases with strip placement angle, corresponding to what is like for ‘ a_1 ’. But, it shows a difference in progressive reduction with respect to roughness height for a_3 (Table 9 (II); Figure 10.3). Furthermore, the absolute value of a_3 undergoes a steep reduction of 95% as the damping is decreased by 55% (Table 9 (III); Figure 10.3); whereas, ‘ a_1 ’ remains nearly the same (undergoes only minimal changes). Figure 10.3 also shows that, for a particular roughness, a_3 increases with strip placement angle under identical damping conditions. Figure 10.3 further reveals that, when the strip placement angle is increased from 20deg. to 40deg., a_1 increases by 16.7% whereas, a_3 becomes nearly double. Overall, it can be easily found that though ‘ a_1 ’ and ‘ a_3 ’ are both set to be the hydrodynamic coefficients of the cross section, present results indicate that ‘ a_1 ’ appears to be a more appropriate representative of the body geometry.

Barrero-Gil et al (2009) calculate the power harnessed by asymmetric cross-sectional cylinder undergoing galloping via. A conversion factor (or efficiency) is defined by the ratio of the power imparted by the flow to the body per unit length and the total power in the flow per unit length, that is

$$\eta = \frac{P_{F-B}}{P_{fluid}} \quad (10.29)$$

where P_{fluid} is defined in Chapter 8 as $1/2\rho U^3 DL$ and P_{F-B} is defined by

$$P_{F-B} = \frac{1}{T} \int_0^T F_y \dot{y} dt \quad (10.30)$$

The efficiency of maximum possible power extraction by the oscillating body under galloping was derived as

$$\eta_{max} = \frac{a_1^2}{6a_3} \quad (10.31)$$

at flow speed equal to two times U^*_{gallop} . η_{max} is decided by both 'a₁' and 'a₃'. Values of both 'a₁' and 'a₃' on circular cylinder with PTC are found to be lesser than those of other conventional galloping-prone sections as delineated in Table 4-3 of (Blevins 1977). All the calculated η_{max} values are listed in Table 20. Two interesting observations can be made:

1. The calculated maximum efficiency indicates that a circular cylinder with PTC applied on 30deg to 46deg and higher surface roughness results in higher efficiency of energy conversion. This result is also verified by the experimental results presented in Section 6.5, Figure 6.10 and Figure 6.11. The most efficient PTC configuration from experimental results is PTC located at 30deg to 46 deg and rougher surface (P60), which shows a consistency across calculated outcomes.
2. Considering all the data gathered in the present study, the maximum possible efficiency of cylinder with PTC is calculated to be about 81% (from the experiment with PTC at 20deg to 36deg, $K=2,000N/m$, $\zeta_{system}= 0.01$), which is higher than the possible value for (a) a typical square section cylinder ($a_1=2.69$ and $a_3=-1.684$; $\eta_{max} =71.6\%$), and (b) a rectangular cylinder ($a_1=1.9142$, $a_3= -170.97$; $\eta_{max} =0.36\%$) and (c) D-section ($a_1=-0.097431$, $a_3=-28.835$; $\eta_{max} =0.005\%$). For square, rectangular and D-sections, these values are calculated at smooth flow conditions based on the data given in Table.4-3 derived from Blevins (1977). This finding highlights the fact that, the ge-

ometry utilized in the present study, viz., and circular cylinder with PTC is very efficient for energy conversion. It is more efficient than some of the conventional mechanisms prone to high amplitude oscillations. This result also bears significant importance for present investigation as one of the primary objectives of this study focuses on power harnessing through FIM, as laid down in the preamble of this dissertation.

3. Furthermore, it is worth noting that the maximum flow incidence angle (Φ_{\max}) increases with the PTC placement angle. In short, the absolute values of Φ_{\max} , a_1 and a_3 altogether register an increasing trend with respect to the placement angle, indicating that they could be hydrodynamically related. However, to reveal the exact relationship between them, further systematic studies are required.

TABLE 19. CALCULATED VALUE OF a_3 WITH VARIED CONFIGURATION OF PTC, STIFFNESS AND DAMPING

(I)

Location	$U^*_{\text{galloping}}$	ReD	A/D at U^*_{gallop}	$\tan\Phi_{\max}$	Slope	a_1	a_3
20-36	9.7	7.897E+04	1.39	0.8980	0.2450	0.0586	-0.0021
30-46	9.08	7.333E+04	1.21	0.8402	0.2146	0.0627	-0.0023
40-56	8.03	6.487E+04	1.39	1.0848	0.0770	0.0708	-0.0043
50-66	7.8	6.205E+04	1.39	1.1168	0.0590	0.0729	-0.1258
64-80	7.5	5.923E+04	0.36	0.2987	N/A	0.0759	N/A

(II)

Roughness	$U^*_{\text{galloping}}$	ReD	A/D at U^*_{gallop}	$\tan\Phi_{\max}$	Slope	a_1	a_3
P150	9.7	7.89E+04	1.3358	0.8653	0.1274	0.0586	-0.0033
P120	9.7	7.89E+04	1.3864	0.8980	0.2450	0.0586	-0.0021
P80	9.7	7.89E+04	1.3864	0.8980	0.2544	0.0586	-0.0021
P60	9.7	7.89E+04	1.3864	0.8980	0.3689	0.0586	-0.0016

(III)

K (N/m)	$\zeta_{\text{structure}}$	U^*_{gallop}	ReD	A/D at U^*_{gallop}	$\tan\Phi_{\max}$	slope	a_1	a_3
400	0.0227	14.5	7.90E+04	1.09	0.47	0.0166	0.0596	-0.0145
600	0.0185	12	7.90E+04	1.23	0.64	0.0664	0.0588	-0.0636
800	0.0160	10.6	8.09E+04	1.22	0.72	0.0890	0.0576	-0.0048
1000	0.0143	9.1	7.33E+04	1.25	0.86	0.0645	0.0600	-0.0053
1200	0.0131	8.7	8.18E+04	1.37	0.98	0.1062	0.0573	-0.0035
1400	0.0121	8.1	8.18E+04	1.43	1.10	0.4769	0.0570	-0.0012
1600	0.0113	7.4	8.18E+04	1.36	1.15	0.6008	0.0583	-0.0009
1800	0.0107	6.8	7.90E+04	1.48	1.36	0.5684	0.0599	-0.0009
2000	0.0101	6.5	7.90E+04	1.33	1.28	0.7979	0.0594	-0.0007

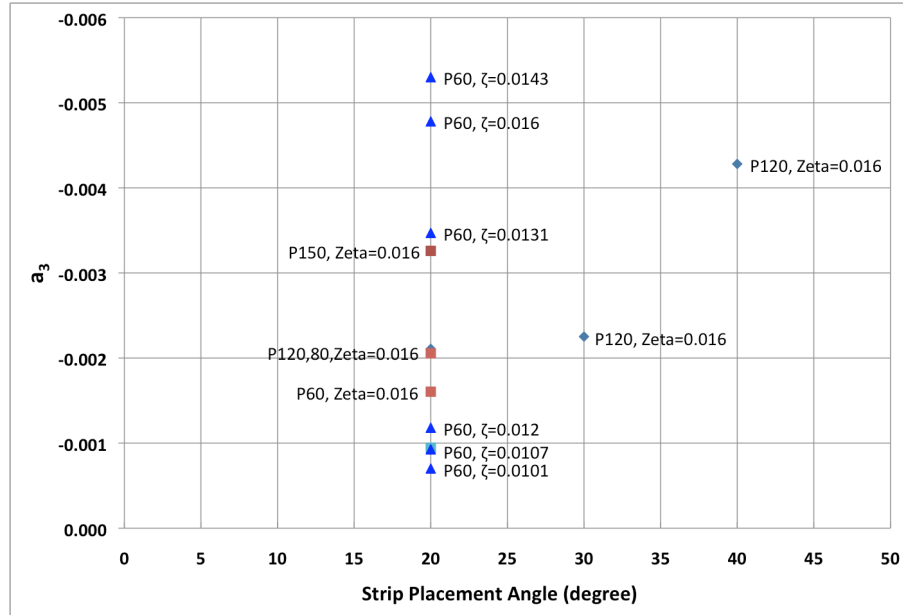


Figure 10.3. Variation of coefficient a_3 with strip placement angle, roughness and damping.

TABLE 20. CALCULATED VALUE OF η_{\max} WITH VARIED CONFIGURATION OF PTC, STIFFNESS AND DAMPING

P120 PTC @ Location	η_{\max} (%)
20°-36°	27.20
30°-46°	29.05
40°-56°	19.53
50°-66°	0.70
64°-80°	N/A

PTC at 20°~36° with Roughness	η_{\max} (%)
P150	17.58
P120	27.20
P80	27.89
P60	35.73

P60 PTC @ 20°~36° with K (N/m)	$\zeta_{\text{structure, damping ratio}}$	η_{\max} (%)
400	0.0227	4.07
600	0.0185	0.90
800	0.0160	11.56
1,000	0.0143	11.32
1,200	0.0131	15.77
1,400	0.0121	45.85
1,600	0.0113	59.95
1,800	0.0107	64.50
2,000	0.0101	83.96

CHAPTER 11

VISUALIZATION OF NEAR WAKE STRUCTURES

11.1. Background

The near wake flow structures around the cylinder in smooth and rough surface conditions (with strips) are presented and discussed in this chapter. The wake structures are given as sketches made from frame-by-frame analysis of video of the flow visualization experiments performed as a part of the present study. The cylinder in motion with flow details are shown in the Figure 7.1 to Figure 7.8 with the corresponding phase of motion expressed as t/T where t is time in the periodic motion and T is the period of oscillation. Only the salient stages of the wake dynamics of the cylinder are illustrated here. It should be noted that the sketches of flow patterns presented are not drawn to scale as they are primarily meant to bring out the qualitative aspects of the flow fields and not any quantitative measures. In the text below, BDC refers to Bottom Dead Center, which is the bottom, most point of cylinder motion and TDC refers to Top Dead Center, which is the top, most point of cylinder motion during an oscillatory cycle.

11.2. Vortex structure of smooth cylinder

At the beginning of the initial branch $U^* = 4.7$, the 2S mode of shedding was clearly observed and is not presented here, as it is a well-known mode of shedding. As the reduced velocity is increased, at $U^* = 5.6$, i.e. at the upper end of the initial branch and beginning of the upper branch, a different mode of shedding was develops in the near wake wherein 7 vortices are shed per cycle of oscillation. The vortex pattern observed in a typical oscillatory cycle is detailed in the sketch sequence shown in Figure 11.1, where vortices are numbered, as V1 to V7, in the order of their genesis in the wake. Red flow lines marked in the flow fields indicate the flow of fluid carrying oppositely signed vor-

ticity across the wake.

As Figure 11.1 shows, two new vortices, V1 by the top shear layer and V2 by the bottom shear layer, are generated at the BDC (Bottom Dead Center) of the oscillatory cycle. As the cylinder traverses up, they grow in size and at the time instant $t/T=0.182$, the top shear layer generates vortex V3. At $t/T=0.227$, the bottom shear generates V4; V2 is shed at the same instant by the action of oppositely signed vorticity as postulated by Gerrard (1966). As upward cylinder motion progresses, both V1 and V4 register continuous growth while moving towards the base of the cylinder. At $t/T=0.363$, the top shear layer forms V5. At $t/T=0.409$, V1 is shed by the formation and pushing by vortex V5 generated by the same shear layer. This passive shedding mechanism was first observed by Raghavan, Ajith.K et al. (2009) for a square section cylinder undergoing forced oscillation. The present result, for a circular cylinder, shows that this shedding mechanism may appear independently of the body geometry. At this instant, V3 is shed along with V1. Motion and shedding of V3 is seen to be quite unique. Soon after its formation, V3 rolls over V1 and crosses over it at $t/T=0.363$ and sheds along with V1. At the same time, V4 continuously grows and rolls up towards the cylinder base. During the process, V5 is shed by Gerrard's mechanism at $t/T=0.682$ after registering significant growth since its formation. Next, top and bottom shear layers introduce vortices V6 and V7. Particular attention should be paid to the genesis of V7 from inside of vortex V4. Such a peculiar formation of vortex appears to be the first of its kind to be reported in the literature (Figure 11.1 (i)); $t/T=0.91$). Equally peculiarly, V7 grows while being inside V4 which pushes V7 away to shed at $t/T=0.91$. Even though the shedding mechanism is similar to that of V1, i.e., passive shedding mechanism, the constitution of the participating vortices is entirely different. In the case of V1, it is subjected to passive pushing by V5, which is an independent vortex but fed by the same shear layer. On the contrary, V7 is formed within V4 and it grows to passively push V4 to be shed. In the mean while, V6 also grows and is shed at BDC along with V7 (not shown here).

Quite clearly, the mode observed does not fit into any of the known shedding modes at lower Reynolds numbers (such as 2S, 2P, P+S, 2C, 2T & 2Q) reported by Williamson and Roshko (1988), Raghavan .and Bernitsas (2010), Williamson and Jauvtis (2004) so

far. However, with regard to the number of vortices shed, the present mode lies in between $2T$ (where 6 vortices are shed per oscillation cycles) and $2Q$ (where 8 vortices are shed per oscillation cycle). It is noted that no vortex pairing was observed in the present case. Significant wake deflections (Figure 11.1(e); $t/T=0.409$) are observed during the oscillatory traverse of the cylinder. Among the vortices, some vortices grew very strong (such as V4 and V5) when compared to the others. Also, some vortices are observed to be nearly circular in shape (eg., V5) whereas others are significantly ‘stretched’ (eg., V6) more or less in the direction of wake axis. This appears to depend on the timing of vortex formation, wake deflection, and proximity and/or association to other vortices.

As reduced velocity is increased throughout the upper branch, more or less 7 vortices are observed per cycle of body oscillation. Even though the number of vortices shed per cycle is nearly invariant along the upper branch, some differences were observed in the wake structures at other reduced velocities. Figure 11.2 shows another case at $U^* = 7.7$. Unlike the case at $U^* = 5.6$ (Figure 11.1 (a); V1 & V2 are newly formed), the top (V2) and bottom (V1) vortices are seen to be grown up at BDC with the occurrence of shedding for V1 (Figure 11.2 (a); $t/T=0$). Wake witnesses the formation of two more vortices V3 and V4 at $t/T=0.125$ (Figure 11.2 (b); $t/T=0.125$), whereas such a similar event occurs at about $t/T=0.2$ for the previous case ($U_r=5.6$). Both V3 and V4 grow along with the upward cylinder motion and subsequently, V3 gets shed at $t/T=0.25$ following Gerrad’s mechanism. The motion and shedding of V3 (Figure 11.2 (b); $t/T=0.125$) is different from that observed in the previous case where V3 rolls over another vortex (V1) and is shed along with V1 (Figure 11.1(b); $t/T=0.182$). Similarly to Figure 11.1, V4 exhibits significant growth while rolling over the cylinder surface towards the base. V4 gets shed at $t/T=0.75$ by the formation and pushing of V7, which is an independent vortex fed by the same shear layer (Figure 11.2 (g)), whereas in the previous case (Figure 11.1), V7 forms and grows inside V4 passively pushing it to get shed (Figure 11.1(h-i)). In the present case, V6 (formed at $t/T=0.75$) rolls up and sheds at $t/T=0.917$ due the passive pushing by V8 (Figure 11.2 (h)). At the corresponding instant, the vortex structure is different from the previous case (Figure 11.1 (i)). Results indicate that, even a slight change of reduced velocity could bring notable changes in the flow structures around the cylinder. As an example, Figure 11.3 shows the near wake structure showing two vortices at $t/T=0.334$

corresponding to a reduced velocity value of 8.03. This is qualitatively different from the wake structure in the previous case ($U^* = 7.7$) where vortex V5 is generated by the top shear layer (Figure 11.2 (d); $t/T=0.333$). Thus, the constitution and shedding timing of the vortices is strongly dependent on the reduced velocity. Consequently, these changes in the wake state are expected to induce changes in the surface pressure distribution and hence on the amplitudes of motion of the cylinder. This observation is consistent with Figure 3.2 and Raghavan & Bernitsas (2010) demonstrating the dependence of VIV on Reynolds number.

In the de-synchronization branch, no definite periodicity was observed in the wake of the cylinder indicating that the shedding process is unlocked from the cylinder motion. Many a times, similar vortices constitute the wake assuming identical configurations about the wake axis as shown in Figure 11.4 ($U^* = 13.8$). Also, the wake was seen to be short and narrow. This is an indication of near-equal pressure distribution on the top and bottom surfaces of the cylinder, which could only result in negligible lift force and consequent small amplitudes of motion. Generally in this case, the vortices are found to be weakly rolled up rightly reflecting the smaller excitation amplitudes observed. The image in Figure 11.4 requires additional explanation since it is very dynamic rather than static as may be conceived from the picture. The vortices that appear attached to the cylinder are not composed of the same fluid particles at all times as would be the case for $1 < Re < 40$. Instead, vorticity sheds continuously out of the narrow wake and new vorticity roles up in the vortices. The inner picture of the wake is that of weak growth and reduction of the two attached vortices alternatively and periodically with continuous inflow and outflow of small-scale vorticity. That is, no large-scale vortices form and shed; all vorticity sheds at small-scale with part of it shedding directly and part through the narrow wake outlet. The outer image is that of an airfoil with fully suppressed VIV.

11.3. Vortex structure of cylinder with PTC in VIV

Synchronization range: The picture-sequence in Figure 11.5 shows the wake development and structure for one full cycle of oscillation at reduced velocity of 7.5, which is selected to represent the synchronization range. The experiment is for roughness strip

P60, with width of 0.5" resulting in coverage of 16° starting at $\alpha_{PTC}=10^\circ$. Starting at BDC, vortices V1 and V2 grow with upward cylinder motion. V1 and V2 are shed at time instances $t/T=0.077$ and 0.27 , respectively (Figure 11.5 (b) and (d)) following Gerrard's mechanism. A third vortex V3 forms from the bottom shear layer at $t/T=0.12$ which grows with time simultaneously moving closer to the cylinder base. V3 exhibits tremendous build up of circulation. Vortex V4 generated by the top shear layer forms at $t/T=0.308$ and sheds at $t/T=0.54$ as depicted in Figure 11.5 (f) by Gerrard's mechanism. After significant growth and partial dissipation, V3 is shed at $t/T=0.731$ by the formation and pushing of V6 passive shedding mechanism. Vortex V5 also forms at this instant ($t/T=0.731$) and is shed at $t/T=0.962$ by Gerrard's mechanism. While the cylinder is getting closer to BDC again, V5 undergoes significant distortion along the direction of the wake axis as shown in Figure 11.5 (i).

A total of 5 vortices are shed per cycle of oscillation; fewer compared to that for smooth cylinder at about the same reduced velocity. The amplitude of oscillation is also lower in this case ($A/D=1.2$ at $U^* \cong 7.5$) than in the smooth cylinder case ($A/D=1.3$ at $U^* \cong 7.5$). In addition, apart from some similarities, the flow structures exhibit some differences also when compared to those of the smooth cylinder case at similar time instances. At $t/T=0.12$, the wake is constituted with V3 newly generated by the bottom shear layer with another growing vortex, V2 not yet shed, in the top shear layer, as illustrated in Figure 11.5(c), whereas at a closely identical time instant, for the smooth cylinder case, the wake carries an additional, new vortex V3 fed by the top shear layer along with vortex V2 which just shed, Figure 11.2 (b); $t/T=0.125$. Differences between the two cases in wake structures are observed at $t/T \sim 0.92$ as well. In the smooth cylinder case, wake encompasses an additional vortex V8 fed by the top shear layer, as in Figure 11.2 (h), unlike the rough cylinder case in Figure 11.5 (j). As expected, surface roughness brings changes in the flow structure around the cylinder leading to changes in the cylinder excitation levels.

When the reduced velocity was further increased to 9.8, the number of vortices shed per cycle increased to 7. Figure 11.6 (a) shows the wake pattern at BDC. At $t/T=0.2$ with the cylinder moving upwards, as Figure 11.6 (b) shows, the wake has developed addi-

tional vortices V3 and V4. Significant wake swing was observed with a downward steep swing. Even at much lower Reynolds numbers, such wake swing is possible for a circular cylinder but of smaller magnitude (Ongoren and Rockwell, 1988). At the corresponding phase of motion, the flow structure is different from that of the lower reduced velocity $U^*=7.5$ case in Figure 11.5 (k), $t/T=0.193$. Further, Figure 11.6 (c) shows the flow pattern when the cylinder traverses downward during the second half of the oscillatory cycle at $t/T=0.851$; vortices V5, V6 and V7 are observed here.

11.4. Vortex structure of cylinder in galloping

Galloping branch: The picture-sequence in Figure 11.7 shows the wake structures around the cylinder at a reduced velocity of 11.53 over a complete cycle of oscillation. While undergoing galloping, the cylinder oscillatory amplitude is very high with $A/D=2.8$ at this reduced velocity. Starting from BDC in Figure 11.7 (a), vortices V3 and V4 are formed on the top and bottom shear layers, respectively. Soon after BDC at $t/T=0.044$ in Figure 11.7 (b), vortices V3 and V4 undergo limited growth before they shed at $t/T=0.1303$ in Figure 11.7 (c). At this instant $t/T=0.1303$, additional vortices V5 and V6 are generated in the shear layers and they shed at $t/T=0.22$ in Figure 11.7 (d) after exhibiting limited growth like V3 and V4. At this same instant $t/T=0.22$, the wake witnesses formation of additional vortices V7 and V8. Interestingly, while V7 sheds at $t/T=0.348$ (not shown here), V8 continues to grow with upward cylinder motion exhibiting significant build up of circulation. V8 rolls up towards the cylinder base as the cylinder moves towards TDC. At TDC, V8 is shed by the formation and pushing of vortex V10 as shown in Figure 11.7 (e) at $t/T=0.5$. The flow of oppositely signed vorticity towards V8 is found to be very weak. Simultaneously with V10 from the bottom shear layer, V9 forms by the top shear layer. After build up of circulation over a period of time, V9 is shed at $t/T=0.697$, in Figure 11.7 (f), whereas, V10 continues to grow in size and finally is shed at $t/T=0.827$ due to the formation and pushing of V12 in Figure 11.7 (g). V11, which is formed at $t/T=0.74$ (sketch not shown) exhibits a slow and steady growth till the cylinder reaches BDC at the same time undergoing some geometrical distortion more or less in the direction of the wake axis.

In this case, a total of 10 vortices shed per cycle of oscillation. It should be noted that there is a notable increase in the number of vortices shed compared to the case in the VIV synchronization range for both the smooth and rough cylinder cases. This indicates that, during galloping, the amount of circulation generated per oscillatory cycle is higher. One peculiar characteristic observed is the simultaneous generation of vortices from the top and bottom shear layers. This was observed repeatedly during the oscillatory cycle, such as V3 and V4 in Figure 11.7 (b). Also, the wake undergoes very high deflections (swings) at some instants of time as in Figure 11.7 (h) at $t/T=0.305$. Among the ten vortices generated in one cycle, V8 and V10 grow substantially stronger than the others. In addition to growing stronger, they persist for a longer time in the wake being closely attached to the cylinder surface. Hence, these vortices could be expected to play a major role in the cylinder dynamics. The cycle analysis performed at a still higher reduced velocity of 12.5 also revealed somewhat similar overall wake characteristics with a total of 10 vortices shed per oscillatory cycle (not presented here). The flow visualization analysis presented in this paper is very tedious due to the challenge of identifying vortices in the flow field at high amplitude, high Reynolds number conditions.

For generation of new vortices, body acceleration could be a major factor (Honji and Taneda, 1969; Williamson and Roshko, 1988). In the present study though, results show (Figure 11.2) that generation of new vortices need not occur at the maximum acceleration position (BDC/TDC) of the cylinder. Both in smooth cylinder and rough cylinder FIM, new vortices are generated at positions of the cylinder other than BDC/TDC as well. It is also worth mentioning that, vortex pairing was not observed in any of the present cases for smooth or rough cylinders within a downstream distance of about $3.5D$. It is possible that, at larger downstream distances (within $15D$), small vortices coalesce to form larger vortices (Williamson and Roshko, 1988) and this could finally culminate in a recovered vortex street with a different structure and frequency (Ongoren and Rockwell, 1988). However, such possible wake transformations at greater downstream distances could not be verified in the present case due to system limitations. Also, as mentioned earlier, significant wake swinging has been observed in the present study, but it has not resulted in vortex pairing contrary to what has been suggested by Williamson and Roshko (1988). A close inspection of the present flow visualization results reveals that, apart from wake

swing, convection velocities of vortices could play an important role in the pairing action. Vortices with nearly equal convection velocities would possibly pair-up. In the present case, almost all of the interacting vortices are found to have unequal convection velocities. Besides this, much higher Reynolds number in the present study have significantly influenced the different vortex dynamics observed.

One of the flow features observed in galloping is that the number of vortices shed per cycle (10 vortices) is higher than that in the VIV synchronization range (7 vortices). This additional, motion-induced vortices, contribute to the occurrence of galloping. This conceptually agrees with the observation of Bokaian and Geoola (1984b) that during galloping vortex shedding frequency increases. As is well known, a smooth circular cylinder is not prone to galloping instability in isolated conditions since the derivative of lift coefficient with respect to flow angle of incidence is zero (Alonso et al., 2009). But, with roughness strips applied to the circular cylinder, the geometry is effectively changed to a non-circular section. Hence, the resulting geometry with roughness strips acts like any other sharp cornered body with fixed flow separation points at the upstream edge of roughness strips. For a non-circular section, the effect of angle of incidence on the flow structure around the body is significant as shown by Parkinson (1971). At reduced velocities below 100, galloping is induced primarily by the effect of angle of incidence (Nakamura et al., 1991). A change in flow incidence angle bring changes in the configuration of shear layers on both sides of the cylinder altering the surface pressure distribution generating additional ‘motion-induced’ forces responsible for galloping (Parkinson and Sullivan, 1979). In the present study, the angle of incidence induces wake structures responsible for galloping. Surface pressure measurements could not be carried out in the present experimental program. However, direct comparison between FIM of smooth and rough cylinders confirm that the pressure distributions resulting from the effect of the angle of attack generate ‘motion-aiding’ forces or in other words generate negative aerodynamic damping causing galloping. Surface pressure distributions enabling the occurrence of galloping have been demonstrated in the literature (Nakamura et al., 1994; Kim, 2009).

Another point to be highlighted is that placement of roughness strips at lower circumferential angles increases the effective after-body length of the cylinder making it

more liable to galloping. For a smooth circular cylinder, the flow separates at about 80° (Achenbach, 1968; Nishimura and Taniike, 2001) and hence, the available after-body length for the pressure fluctuations to be felt is shorter. This is evidenced in Figure 3.2 where, for strip placement angles less than about 64° , persistent galloping has been observed and for angle 64° , oscillations drastically dropped off to negligible levels. Like for other non-circular sections (Alonso et al., 2005) a transient separation bubble could be expected to form around a sharp corner (roughness strips), which would grow with increasing angle of attack till it collapses at the critical incidence angle giving rise to a fully separated flow. At that point, galloping is likely to commence. Finer flow details very close to the roughness elements were not captured in the present investigation.

A PIV study of the flow field along with surface pressure measurement is expected to shed more light into the physics of galloping excitation observed in the present study and this is planned for the future. As detailed in the aforementioned section, flow visualization experiments were conducted mainly to distinguish the vortex wake structures during VIV and galloping. This qualitative study could not be extended further to specifically cover the effect of roughness height, strip location, and strip area coverage on the response features of the cylinder. Such extensive studies are also planned for the future.

11.5. Comparison with William-Roshko map

The amplitude (A/D) versus reduced velocity (based on the oscillation frequency) for a smooth cylinder is re-plotted on the Williamson-Roshko map and is shown in Figure 11.8. The initial branch and part of the upper branch pass through the 2P regime of the map. The later part of upper branch crosses over to the region of no-synchronized wake pattern of the map. In the 2P region of the map, no such patterns are majorly observed in the present study. Instead, 7 vortices are independently shed per cycle of oscillation without the occurrence of vortex pairing. In terms of number of vortices, this could be considered as equivalent to '2T+S' mode of shedding. Similar is the case of vortex structures observed in the later half of the upper branch, which lies in the 'no-synchronized wake pattern' zone of the map.

This deviation of the present results from the map is another indication of the possible Reynolds number effect on the mode of shedding. The Williamson-Roshko map was constructed using experimental results taken at Reynolds numbers less than 1000, whereas the present results pertain to a Reynolds number range $10^4 \leq Re \leq 10^5$. The cylinder oscillations in this study are found to be stable and periodic throughout the upper branch. Displacement wave forms of cylinder oscillation at a reduced velocity based on the body oscillation frequency of 7.3 falling in the '2P' zone, and also at a reduced velocity of 8.5 falling in the 'no-synchronized wake patterns zone of the map are shown in Figure 11.8. In light of the present results, it is argued that the validity of the map is possibly limited to low Reynolds numbers. Recent results by Morse and Williamson (2009) show that the Williamson-Roshko map could be valid up to a Re value of 12,000 and not beyond. It should be noted that Raghavan and Bernitsas (2008, 2010) have demonstrated the dependence of VIV on Reynolds number for $30,000 < Re < 120,000$. Recently, Bearman (2009) commented on the possibility of Reynolds number effects in VIV. This dependence on Reynolds number was further evidenced in the present study.

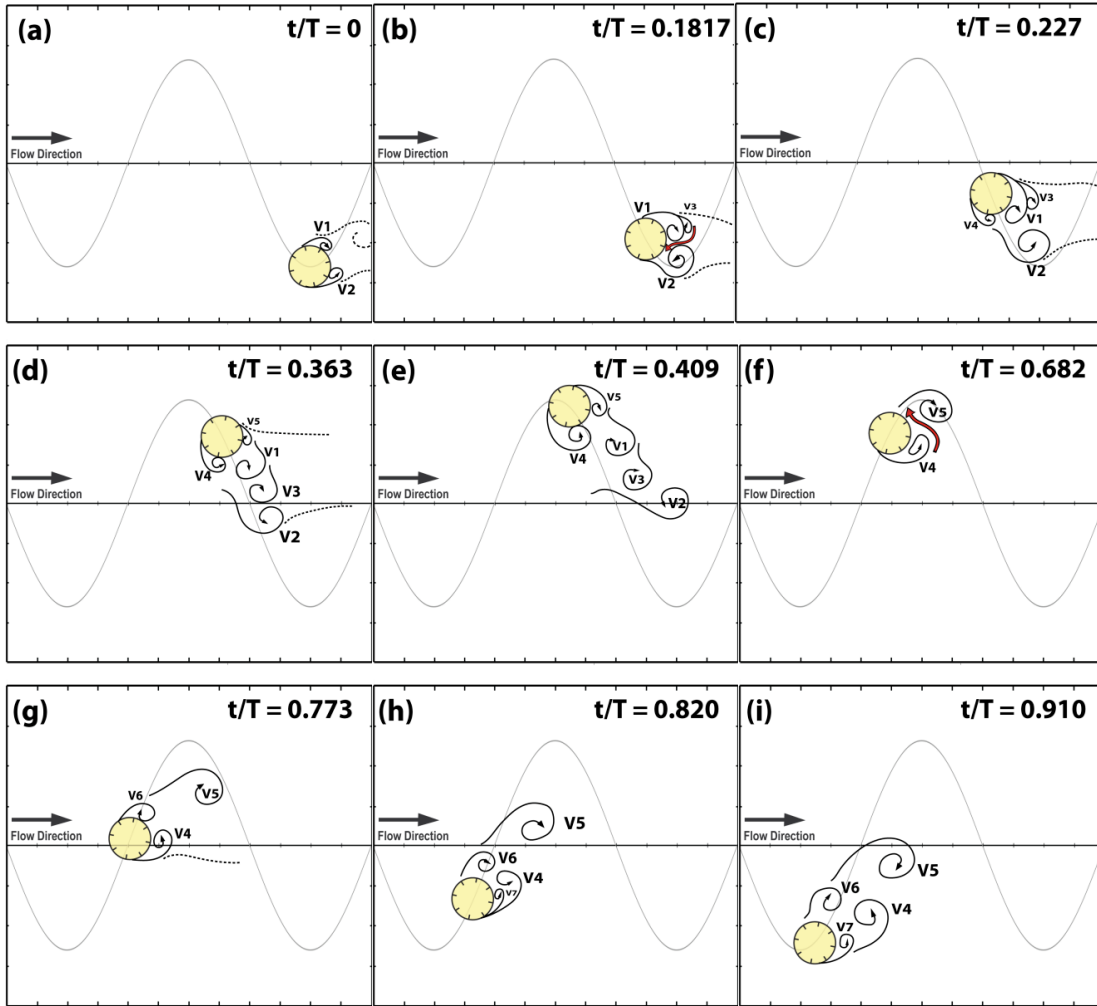


Figure 11.1. Wake structures of smooth circular cylinder at $U^* = 5.6$ (upper end of initial branch)

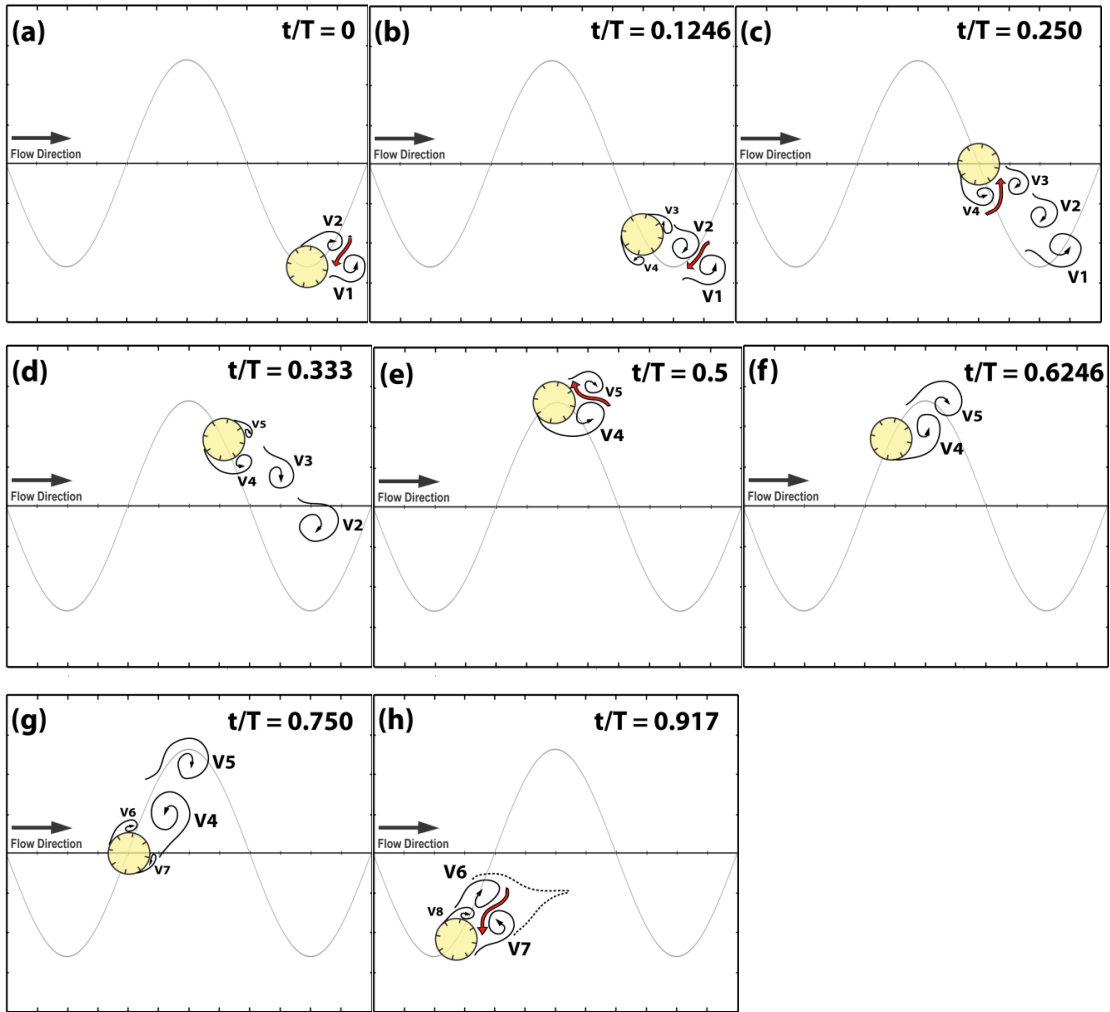


Figure 11.2. Wake structures of smooth circular cylinder at $U^* = 7.7$ (upper branch)

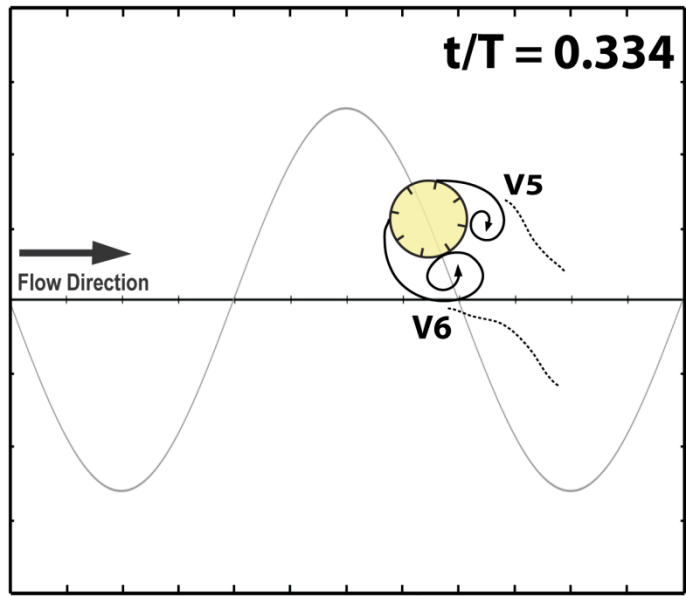


Figure 11.3 Wake structures of smooth cylinder at $U^* = 8.03$ (upper branch)

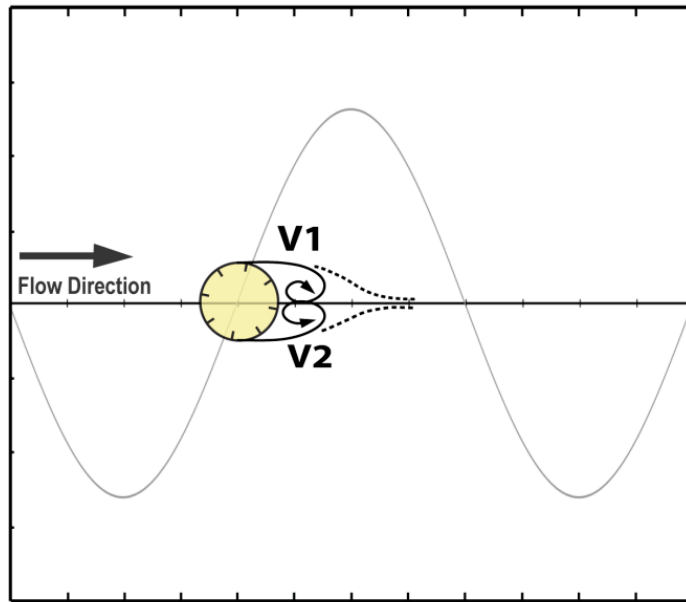


Figure 11.4. Wake structure of smooth circular cylinder at $U^* = 11.8$ (de-synchronization branch).

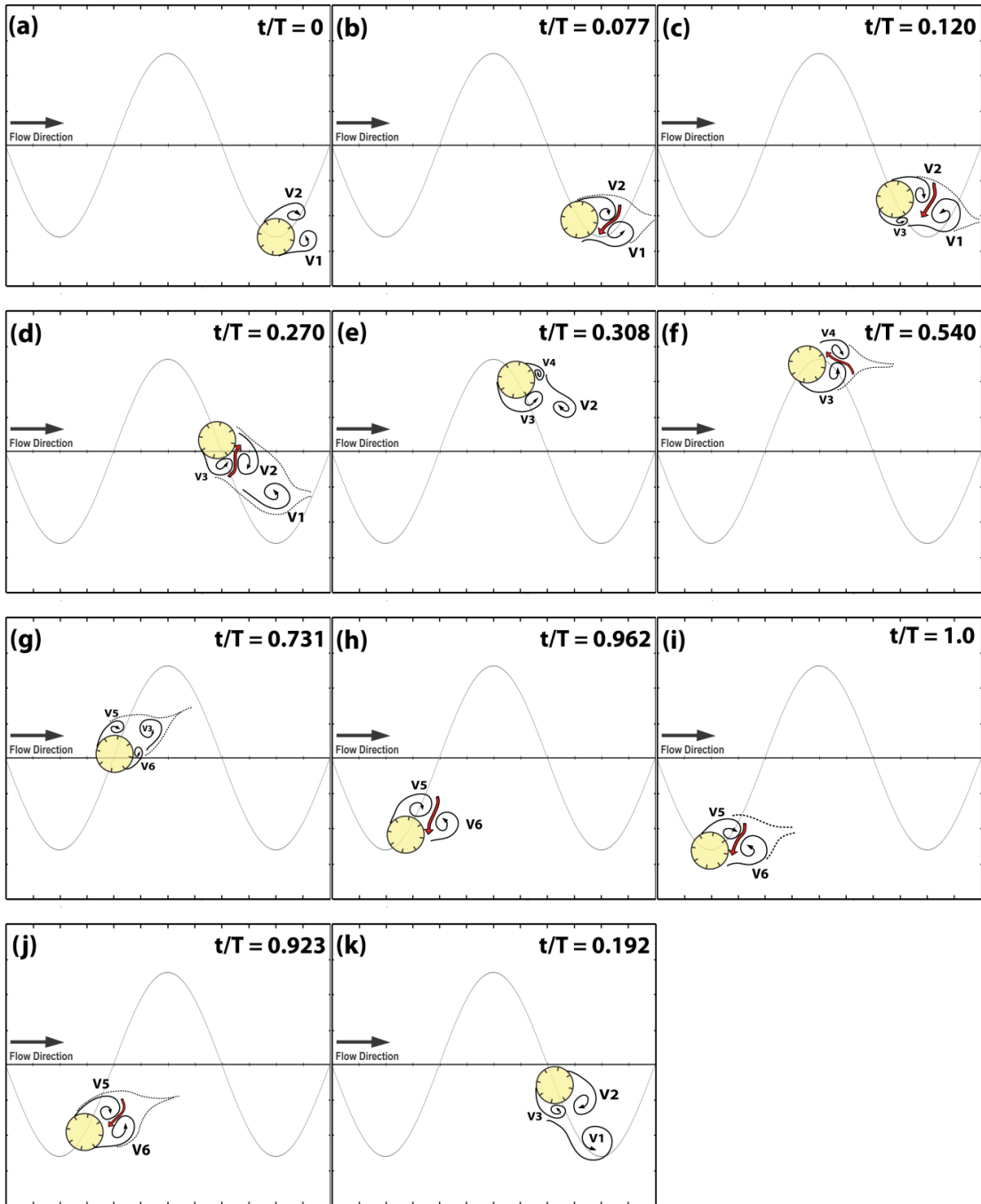


Figure 11.5. Flow structures of a rough circular cylinder at $U^* = 7.5$, VIV synchronization range.

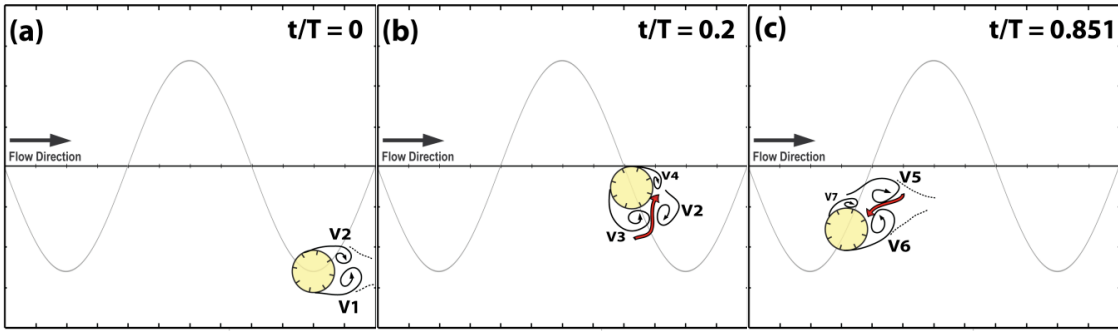


Figure 11.6. Flow structures around the rough cylinder at $U^* = 9.8$ (End of VIV).

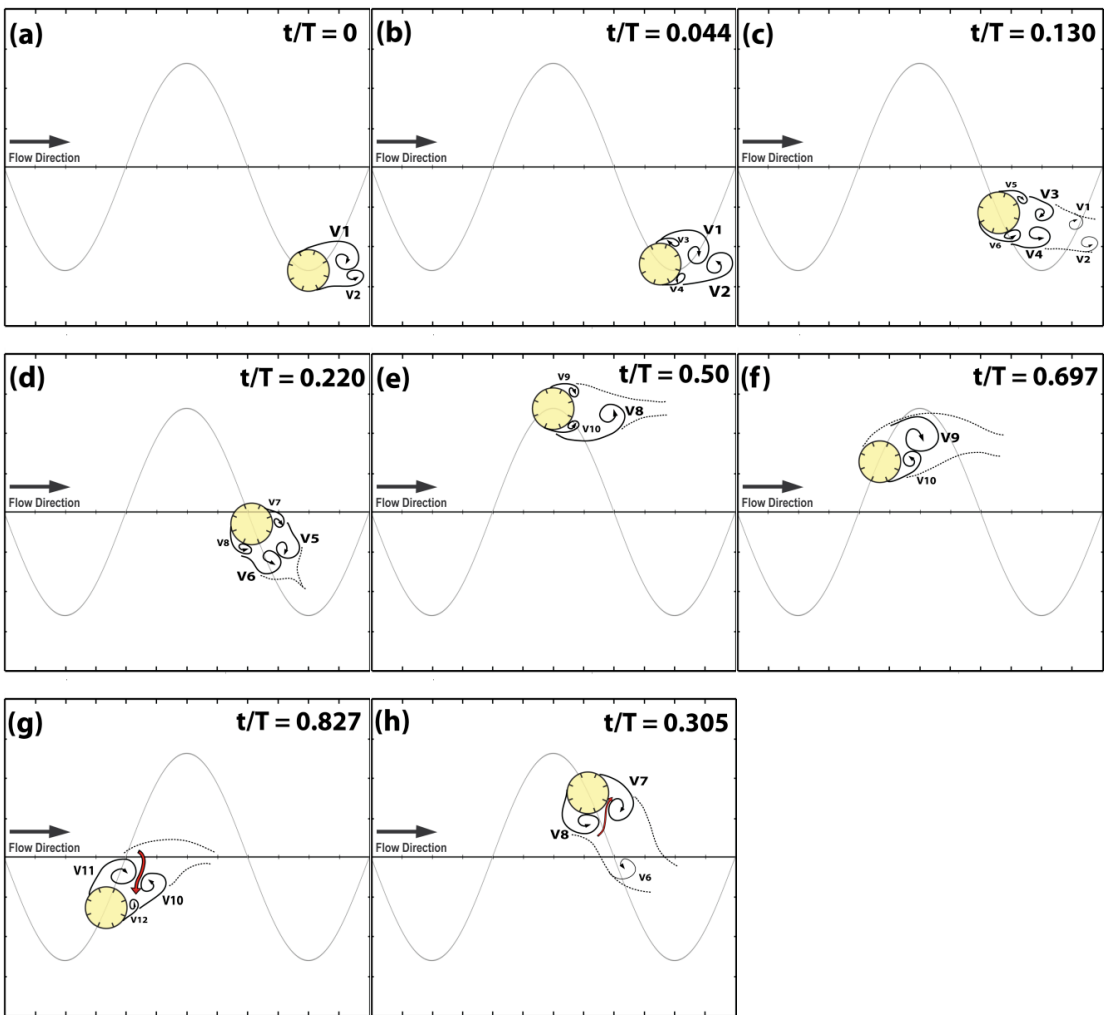


Figure 11.7. Flow structure around rough cylinder at $U^* = 11.53$ (Gallop branch).

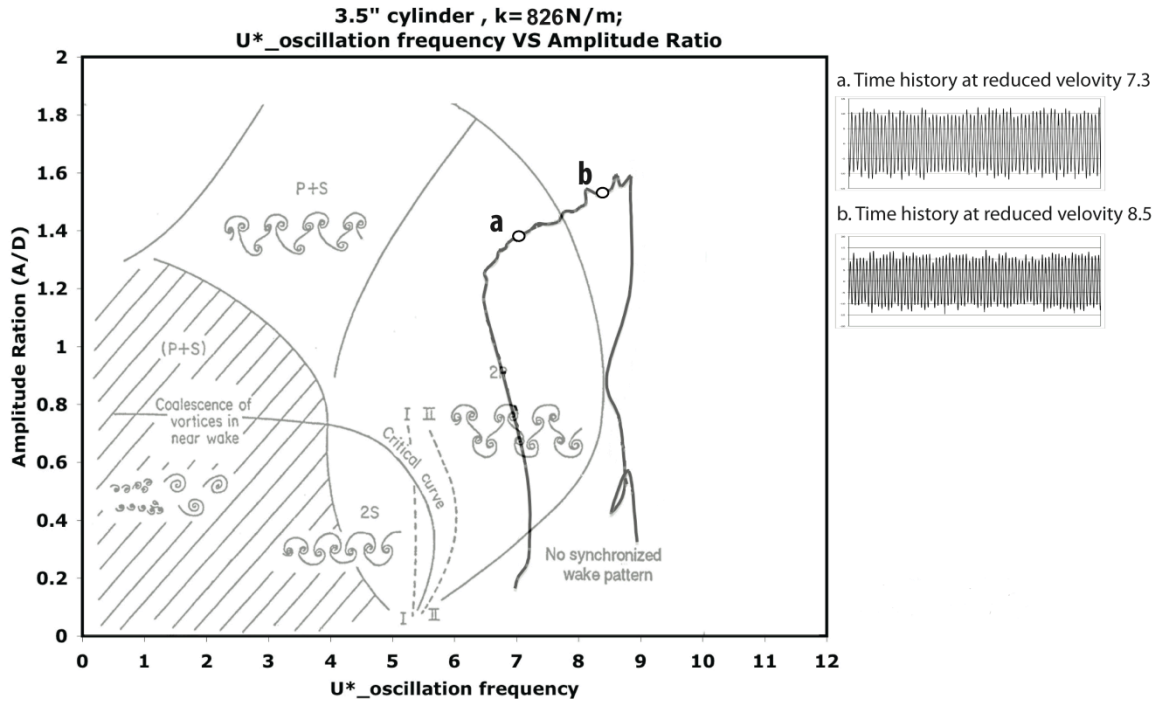


Figure 11.8. Smooth cylinder response at $10^4 \leq Re \leq 10^5$ superposed on the Williamson-Roshko Map

CHAPTER 12

CONCLUSIONS AND RECOMMENDATIONS TO FUTURE WORK

Final conclusions drawn from this research are presented in this chapter along with suggestions for future directions to improve further the efficiency of the VIVACE Converter as well as on its FIM dynamics. Research results derived in this work reveal possibilities to extract greater energy from fluid flow by virtue of high amplitude galloping oscillations besides VIV. Moreover, this investigation brings to light that some of the key features of flow mechanism on a circular cylinder with roughness (PTC) in specific location in this study are precedent and have not been thoroughly examined before. Higher power harnessing at high damping conditions in the VIVACE model is achieved and presented in this dissertation and it provides a foundation for future explorations on renewable energy from the academia as well as the commercial industry.

12.1. Conclusions

In this research, tests were systematically conducted on the VIVACE apparatus primarily designed to generate power from fluid flow. VIVACE is essentially a circular cylinder mounted on real or virtual springs exposed to fluid flow perpendicular to the cylinder axis. As detailed in Chapter 2, the cylinder geometry is altered to an effective non-circular section, which is prone to galloping instability. This geometrical alteration is brought about by attaching straight roughness strips along the entire span of the cylinder. The flow induced motions of the spring-cylinder system, i.e., VIVACE, were investigated at high Reynolds number conditions ($10^4 < Re < 10^5$). For rough surface conditions, straight roughness strips (PTC) with specific width are applied at various circumferential locations on the surface of the cylinder.

Following are the major conclusions derived from this dissertation:

1. In our experiments, the smooth cylinder response exhibits typical VIV characteristics yet it contains differences from what has been previously reported in the open literature. For instance, in the upper branch of the response, the amplitude variation with respect to reduced velocity is nearly linear, contrary to the bell-shaped profile reported by Khalak and Williamson (1999) and Govardhan and Williamson (2000). Further, the upper branch in this VIV response is much broader overtaking most of the VIV synchronization range. In fact, as Bernitsas et al. (2008) reported, the upper branch fully overtakes the lower branch for the VIV response in the VIVACE Converter. In addition to the different profiles of upper branch, the lower branch amplitude decreases steadily in this VIV response, which is in contrast to the nearly flat and broader profile observed by Khalak and Williamson (1999) and the precipitous drop with no lower branch observed by Bernitsas et al. (2008). Unlike previous studies, a small kink is also observed at the beginning of the lower branch in this VIV response, indicated by $U^*=11.0$. These differences were attributed to the difference in Re. Bernitsas et al. experimented around $Re=120,000$ that is in the TrSL3 regime compared to $Re=3600$ where Williamson et al. experimented.
2. At high Reynolds numbers ($10^4 < Re < 10^5$) with Passive Turbulence Control, amplitudes as high as three times of the cylinder diameter were achieved during galloping. Over a broad range of strip placement angle, galloping is observed. Up to a reduced velocity U^* of about 10, the cylinder experiences VIV. Thereafter, galloping occurs for $U^* > 10$. The oscillation frequency is found to decline sharply for all rough cylinder cases at $U^* \sim 10$, indicating the onset of galloping oscillations. Galloping being initiated at this critical reduced velocity ($U^* \sim 10$) manifests fully over a range of reduced velocity. That is, the excitation change over from VIV to fully developed galloping occurs over a range of reduced velocity. Within a broad range of strip location ($20^\circ \sim 64^\circ$), the roughness strip partially suppresses VIV for $U^* < 10$, while inducing galloping for $U^* > 10$. Correspondingly, the oscillation frequency increases with an increasing strip placement angle.
3. Beyond a strip placement angle of about 64° , the roughness strip significantly suppresses VIV while eliminating galloping oscillations. In addition, the oscillation fre-

quency sharply declines in the de-synchronization branch $U^* > 7$ for this case. Similarly, for reduced strip placement angles ($0^\circ \sim 16^\circ$), galloping oscillations are suppressed. In the light of the result that galloping is observed for strip angle $10^\circ \sim 26^\circ$, the strip placement angles $0^\circ \sim 10^\circ$ and $\sim 64^\circ$ are inferred as ‘critical’ locations for the galloping occurrence. Nevertheless, roughness height does not significantly influence both the amplitude and frequency response in the VIV synchronization branch (except minor modifications) but it promotes early galloping. However, the maximum galloping amplitude is not affected by the roughness height.

4. Up to a limiting width, an increase in strip width (strip area coverage) reduces the amplitudes in the VIV synchronization range while it steepens the galloping branch. A further increase in strip width results in significant reduction of both, VIV and galloping amplitudes, with a clear separation between these two phenomena. The oscillation frequency is virtually unaffected by the strip area coverage.
5. Similarly, for cylinders with smooth strips (zero roughness), alike oscillatory features as those with rough strips are observed except for one distinctive difference: for smooth strips, galloping occurs only if the strip thickness is greater than a specific value. Studies with smooth strips brought to light the fact that roughness is not necessary to initiate high amplitude galloping instability whereas the paper thickness of the strip essentially does. Generally, in the majority of all cases, the strips (rough or smooth) induce slightly early onset of oscillations.
6. A higher damping subdues amplitude of oscillation while all other parameters remain the same. A thicker PTC enables a higher power production at higher U^* values. Apart from the magnitude of PTC roughness, its location plays an important role in the oscillatory amplitude and frequency features of the cylinder. There appears to be an optimal PTC location (circumferential angle measured from the front stagnation point), which can contribute to higher power output occurring at higher reduced velocities. At lower reduced velocities, on the other hand, the power output is much lower and is not significantly different from that of the smooth cylinder irrespective of the roughness value. In addition, cylinder with smooth PTC (zero roughness) also delivers power output similar to rough cylinders. This indicates that roughness is not

mandatory to promote higher power generation but it certainly displays as a desirable factor.

7. Contrary to earlier reported results, major shedding mode observed is not of conventional type, such as 2P. In VIV synchronization range (smooth cylinder), about seven vortices are shed per cycle; however, for rough cylinder, it reduces to about five vortices per cycle. This is probably due to the lower amplitude values observed in the VIV synchronization range for all the rough cylinder cases. Interestingly, a higher number of vortices are found to be shed in the galloping branch, ten vortices per cycle. The wake structures during galloping are found to be significantly different from those of the VIV branch.
8. The mathematical modeling derived for the oscillatory system of the cylinder with PTC, yields two hydrodynamic coefficients (a_1 and a_3) following a quasi-steady analysis. The first hydrodynamic coefficient (a_1) determines the critical reduced velocity for galloping. Among the coefficients, a_1 appears to be the best representative of the body geometry. Furthermore, a_1 is nearly invariant with respect to the roughness height but it increases with greater strip placement angle. The absolute value of a_3 also increases with strip location as has been demonstrated in a_1 . Meanwhile, unlike a_1 , a_3 considerably varies with roughness height; the rougher the strip, the smaller is the absolute value of a_3 . Furthermore, a_3 varies with damping ratio; the higher the damping ratio, the higher is the absolute value of a_3 . In sum, the coefficients a_1 and a_3 are derived at critical reduced velocity for galloping. But, the present cylinder response shows that VIV can also coexist with galloping. Therefore, values of these coefficients should be considered as only approximate.
9. The cost-effectiveness of VIVACE on smooth cylinder has been proven by Kamal (2007). Comparison between VIVACE on smooth cylinder with other alternative energy sources including wind, solar, landfill gas new, landfill gas expansion, and Anaerobic Digester, shows that the VIVACE Converter has the lowest cost per kW per hour. VIVACE with PTC further increases the device efficiency by 1.8 times greater than VIVACE on smooth cylinder under velocity of 1.45 m/s. Moreover, VIVACE

with PTC does not increase the fixed cost of the system design, as the cost added by the PTC is practically negligible. In fact, with such an increase in efficiency, VIVACE with PTC will further lower the average cost per kW generated.

12.2. Suggestions and recommendations to future work

1. One of the major limitations encountered in the present study is the physical limitation of the VIVACE system itself. Occasionally during galloping oscillations, the cylinder hits the stoppers, which prevent further advancement of cylinder motions. Hence, experiments can be carried out further by eliminating this hurdle with an increased depth of the water channel test-section. Additionally, using a higher Reynolds number, than what has been achieved in the present study, remains an area for system improvement.
2. Better system configurations could be achieved by modifying the PTC design and its application on the cylinder to generate high amplitude galloping much earlier than (that is at a still lower reduced velocity) what has been achieved in the present study.
3. Extended studies with smooth strips are highly recommended, since it is expected to operate better in ocean environment possibly without fouling compared to the strips with embedded roughness.
4. By utilizing the virtual CK-system, influences of various parameters such as spring stiffness and damping can be further investigated at greater depths, enabling better system optimization.
5. The flow visualization study conducted as a part of the present investigation has limitations though it has provided valuable insights to the wake structures around the cylinder under various flow conditions and PTC configurations. Better visualization, particularly near the separation point, can be carried out in future studies, using PIV techniques, which also serve to compute the velocity vectors. Using PIV, the vortic-

ity distribution can be studied in a greater detail to explain many finer oscillatory features of the cylinder particularly related to galloping.

6. Lift and drag measurements on the cylinder can be carried out by adequately updating the apparatus. Additional reduction of phase difference - between force and displacement - under various flow conditions particularly during galloping will reveal more lift into the system dynamics.

The VIVACE apparatus employed in the present study is the simplest possible configuration. In the process of advancement towards practically feasible VIVACE for power generation, a greater number of cylinders needs to be incorporated starting with a two-cylinder VIVACE system. Indeed, the enhanced system is going to be greatly complicated both from the design as well as the fluid mechanics point of view. Yet, it will be worth to pursue advanced studies on such an elaborated VIVACE system, as it will be a promising commitment to meet the future energy requirements.

BIBLIOGRAPHY

1. Achenbach E., E. Heinecke. "On vortex shedding from smooth and rough cylinders in the range of Reynolds numbers from $6 \cdot 10^3$ to $5 \cdot 10^6$." J. Fluid Mech. 109 (1981): 239-251.
2. Achenbach, E. "Influence of surface roughness on the cross-flow around a circular cylinder." Journal of Fluid Mechanics 46 (1971): 321-335.
3. Achenbach, E., and Heinecke. "On vortex shedding from smooth and rough cylinders in the range of Reynolds number 6×10^3 to 5×10^6 ." Journal of Fluid Mechanics 109 (1981): 239-251.
4. Achenbach, E., and Heinecke. "On vortex shedding from smooth and rough cylinders in the range of Reynolds number 6×10^3 to 5×10^6 ." Journal of Fluid Mechanics 109 (1981): 239-251.
5. Akilli, H., Akar, A., Karakus, C. "Flow characteristics of circular cylinders arranged side-by-side in shallow water." Flow Measurement and Instrumentation 15 (2004): 187-197.
6. Alonso G., Valero E., Meseguer J. "An analysis on the dependence on cross section geometry of galloping instability of two dimensional bodies having either biconvex or rhomboidal cross sections." European Journal of Mechanics B/Fluids 28 (2009): 328-334.
7. Alonso, G., Valero, E., Meseguer, J. "An analysis on the dependence on cross section geometry of galloping stability of two-dimensional bodies having either biconvex or rhomboidal cross sections." European Journal of Mechanics B/Fluids 28 (2009): 328-334.
8. Bahmani, M.H., Akbari, M.H. "Effects of mass and damping ratios on VIV of a circular cylinder." Ocean Engineering 37 (2010): 511-519.
9. Barrero-Gil, A., Alonso, G., Sanz-Andres, A. "Energy harvesting from transverse galloping." Journal of Sound and Vibration, 2010: 1-11.
10. Barrero-Gil, A., Sanz-Andres, A., Roura, M. "Transverse galloping at low Reynolds numbers." Journal of Fluids and Structures 25 (2009): 1236-1242.
11. Batten, W.M.J., Bahaj, A.S., Molland, A.F., Chaplin, J.R. "Hydrodynamics of marine current turbines." Renewable Energy 31 (2006): 249-256.
12. Bearman, P.W. "Understanding and predicting vortex-induced vibrations." Journal of Fluid Mechanics (Cambridge University Press) 634 (2009): 1-4.

13. Bearman, P.W. "Vortex shedding from oscillating bluff bodies." Annual Review of Fluid Mechanics 16 (1984): 195-222.
14. Bearman, P.W. "Vortex Shedding from Oscillating Bluff Bodies." Annual review of fluid mechanics 16 (1984): 195-222.
15. Bernitsas M. M., Raghavan K. Appendages for Enhancement of Vortex Induced Forces and Motion for Hydrokinetic Energy Conversion. U.S. Provisional Patent Application, United States Patent and Trademark Office Patent UofM#3906. May 24, 2007.
16. Bernitsas M. M., Raghavan K. Enhancement of Vortex Induced Forces & Motion through Surface Roughness Control. U.S. Provisional Patent Application, United States Patent and Trademark Office Patent UofM#3737. May 05, 2007.
17. Bernitsas M. M., Raghavan K., Duchene G. "Induced Separation and Vorticity Using Roughness in VIV of Circular Cylinders at $8 \times 10^3 < Re < 1.5 \times 10^5$." OMAE'08. Estoril, Portugal, 2008. 15-20.
18. Bernitsas M.M., Ben-Simon Y., Raghavan K., Garcia E. M. H. "The VIVACE Converter: Model Tests at Reynolds Numbers Around 105." Journal of Offshore Mechanics and Arctic Engineering 131, no. 1 (February 2009): 1-13.
19. Bernitsas M.M., Raghavan k. Converter of Current, Tide, or Wave Energy. U.S. Provisional Patent Application, United States Patent and Trademark Office Patent 7,493,759 B2. February 24, 2009.
20. Bernitsas M.M., Raghavan K., Ben-Simon, Y., Garcia E. M. H. "VIVACE (Vortex Induced Vibration Aquatic Clean Energy): A New Concept in Generation of Clean and Renewable Energy from Fluid Flow." Journal of Offshore Mechanics and Arctic Engineering 130, no. 4 (November 2008): 041101-15.
21. Bernitsas M.M., Raghavan K., Maroulis D. "Effect of Free-Surface on VIV for Energy Harnessing at $8 \times 10^3 < Re < 1.5 \times 10^5$." International Conference on Offshore Mechanics and Arctic Engineering. San Diego, 2007.
22. Bernitsas, M. M. and Raghavan, K. Fluid motion energy converter. United States Patent 60/628,152, 60/244,749. 2005.
23. Bernitsas, M. M., Raghavan, K., and Duchene, G. "Induced separation and vorticity using roughness in VIV of circular cylinders at $8 \times 10^3 < Re < 1.5 \times 10^5$." 27th International OMAE'08 Conference. Estoril, 2008.
24. Bernitsas, M.B.S. "The VIVACE converter: model tests at high damping and Reynolds number around 10^5 ." JOMAE, 2009: 1-13.
25. Bernitsas, M.M. and Raghavan, K. "Converter of current/tide/wave energy", . United States Patent 60/628,252. 2004.
26. Bernitsas, M.M., Ben-Simon Y., Raghavan, K., and Garcia, E.M.H. "The VIVACE converter: model tests at high damping and Reynolds number around 10^5 ." 131, no. 1 (February 2009): 1-13.

27. Bernitsass, M.M., Raghavan, K., Ben-Simon, Y., and Garcia, E.M.H. "VIVACE (Vortex Induced Vibration Aquatic Clean Energy): a new concept in generation of clean and renewable energy from fluid flow." *Journal of Offshore Mechanics and Arctic Engineering* 130, no. 4 (November 2008): 1-15.
28. Bishop, R.E.D., Hassan A.Y. "The lift and drag forces on a circular cylinder in a flowing fluid." *Royal Society of London. Series A, Mathematical and Physical sciences* 277 (1964): 32-50.
29. Bishop, R.E.D., Hassan A.Y. "The lift and drag forces on a circular cylinder oscillating in a flowing fluid." *Royal Society of London. Series A, Mathematical and Physical Sciences* 277 (1964): 51-75.
30. Blevins, R.D. *Flow-induced Vibration*. 2nd. Van Nostrand Reinhold, NY, 1990.
31. Blevins, R.D., Coughran, C.S. "Experimental investigation of vortex-induced vibration in one and two dimensions with variable mass, damping, and Reynolds number." *Journal of Fluids Engineering* 131 (2009).
32. Bokaian, A. "Galloping of a circular cylinder in the wake of another." *Journal of Sound and Vibration* 128, no. 1 (1989): 71-85.
33. Bokaian, A., Geoola, F. "Wake-induced galloping of two interfering circular cylinders." *Journal of Fluid Mechanics* 146 (1984): 383-415.
34. Bokaian, A.R., Geoola, F. "Hydroelastic instabilities of square cylinders." *Journal of Sound and Vibration (Academic Press Inc.)* 92, no. 1 (1984): 117-141.
35. Bruno, L., Fransos, D., Coste, N., Bosco, A. "3D flow around a rectangular cylinder: a computational study." *Journal of Wind Engineering and Industrial Aerodynamics*, 2009: 1-14.
36. Chang, C. C. (Jim), Raghavan A. K., Bernitsas M. M. "VIV and Galloping of Single Circular Cylinder with Surface Roughness at $3.0 \times 10^4 \leq Re \leq 1.2 \times 10^5$." *Ocean Engineering*, april 2010.
37. Cheng, L, Zhou, Y., Zhang, M.M. "Controlled vortex-induced vibration on a fix-supported flexible cylinder in cross-flow." *Journal of Sound and Vibration* 292 (2006): 279-299.
38. Cheng, M., Liu, G.R. "Effect of afterbody shape on flow around prismatic cylinders." *Journal of Wind Engineering and Industrial Aerodynamics* 84 (2000): 181-196.
39. Corless, R.M, Parkinson, G.V. "A model of the combined effects of vortex-induced oscillation and galloping." *Journal of Fluids and Structures* 2 (1988): 203-220.
40. Coton, T. "Unsteady wake-boundary layer interaction on advanced high lift low pressure turbine airfoils."
41. Dahl J. M., Hover F. S., Triantafyllou M. S., and Oakley O. H. "Dual Resonance in Vortex Induced Vibrations at Subcritical & Supercritical Reynolds Numbers." *J. Fluid Mechanics* 643 (2010): 395-424.

42. Deshkulkarni, B.H.Lakshmana Gowda and K.P. "Interference effects on the flow-induced vibration of a circular cylinder in side-by-side and staggered arrangement." *J.Sound & Vibration* 112 (1988): 465-478.
43. Ding, Z.J., Balasubramanian, S., Lokken, R.T., Yung, T.W. "Lift and damping characteristics of bare and straked cylinders at riser scale Reynolds numbers." *Offshore Technology Conference*. Houston, TX, 2004. 1-9.
44. Dipankar, A., Sengupta, T.K. "Flow past a circular cylinder in the vicinity of a plane wall." *Journal of Fluids and Structures* 20 (2005): 403-423.
45. Dunn, W., Tavoularis, S. "Experimental studies of vortices shed from cylinders with a step-change in diameter." *Journal of Fluid Mechanics* 555 (2006): 409-437.
46. Etienne, S. "Vortex induced vibrations and galloping of two cylinders placed in tandem arrangement." *Vancouver, BC, Canada: The Eighteenth International Offshore and Polar Engineering Conference*, 2008.
47. Gabbai, R.D., Benaroya, H. "An overview of modeling and experiments of vortex-induced vibration of circular cylinders." *Journal of Sound and Vibration* 282 (2005): 575-616.
48. Gal, P.L., Croquette, V. "Visualization of the space-time impulse response of the subcritical wake of a cylinder." *Physical Review* 62, no. 3 (2000): 4424-4426.
49. Gerrard, J.H., "The mechanics of the formation region of vortices behind bluff bodies." *Journal of Fluid Mechanics* 25 (1966): 401-413.
50. Gete, Z. "A study of unsteady wake-boundary layer interaction in turbomachines." *The University of British Columbia*, October 1996.
51. Gilbert, S., Sigurdson, L. "Hydrogen bubble flow visualization of a self-oscillating cylinder vortex street "void"." *Physics of Fluids* 17 (2005).
52. Govardhan, R., Williamson, C.H.K. "Mean and fluctuating velocity fields in the wake of a freely-vibrating cylinder." *Journal of Fluids and Structures* 15 (2001): 489-501.
53. Govardhan, R., Williamson, C.H.K., "Modes of vortex formation and frequency response of a freely vibrating cylinder." *Journal of Fluid Mechanics* 420 (2000): 85-130.
54. Govardhan, R.N., Williamson, C.H.K. "Defining the 'modified Griffin plot' in vortex-induced vibration: revealing the effect of Reynolds number using controlled damping." *Journal of Fluid Mechanics* 561 (2006): 147-180.
55. Guven, O., Farrell, C., and Patel, V.C. "Surface-roughness effects on the mean flow past circular cylinders." *Journal of Fluid Mechanics* 98 (1980): 673-701.
56. Hasan, A.B.M.T., Das, D.K. "Numerical investigation on the effects of vortex shedding on boundary layer unsteadiness." *Journal of Mechanical Engineering ME37* (June 2007): 33-39.
57. Hover, F. S., Techet, A. H., and Triantafyllou, M. S. "Forces on oscillating uniform and tapered cylinders in crossflow." *Journal of Fluid Mechanics*, 1998: 97-114.

58. Hover, F. S., Tvedt, H., and Triantafyllou, M. S. "Vortex-induced vibrations of a cylinder with tripping wires." *Journal of Fluid Mechanics* 448 (2001): 175-195.
59. Hover, F.S., Techet, A.H., Triantafyllou, M.S. "Forces on oscillating uniform and tapered cylinders in crossflow." *Journal of Fluid Mechanics* 363 (1998): 97-114.
60. Hover, F.S., Triantafyllou, M.S. "Galloping response of a cylinder with upstream wake interference." *Journal of Fluids Structures* 15 (2001): 503-512.
61. Huang, R.F., Chen, J.M., Hsu, C.M. "Modulation of surface flow and vortex shedding of a circular cylinder in the subcritical regime by a self-excited vibrating rod." *Journal of Fluid Mechanics* 555 (2006): 321-352.
62. Inc., Blue Energy Canada. 2000. www.bluenergy.com (accessed January 2010).
63. Jauvtis, N., Govardhan, R., Williamson, C.H.K. "Multiple modes of vortex-induced vibration of a sphere." *Journal of Fluids and Structures* 15 (2001): 555-563.
64. Jubran, B.A., Hamdan, M.N., Bedoor, B.O.A. "Roughness and turbulence intensity effects on the induced flow oscillation of a single cylinder." *Applied Scientific Research* 49 (1992): 101-115.
65. Khalak, A., Williamson, C.H.K. "Dynamics of a hydroelastic cylinder with very low mass and damping." *Journal of Fluids and Structures* 10 (1996): 455-472.
66. Khalak, A., Williamson, C.H.K. "Fluid forces and dynamics of a hydroelastic structure with very low mass and damping." *Journal of Fluids and Mechanics* 11 (1997): 973-982.
67. Khalak, A., Williamson, C.H.K. "Motion forces and mode transitions in vortex-induced vibrations at low mass-damping." *Journal of Fluids and Structures* 13 (1999): 813-851.
68. Kim, H. "Mechanism of wake galloping of two circular cylinders." Nagoya, Japan: Nagoya University, August 2009.
69. Kim, S., Alam, M.M., Sakamoto, H., Zhou, Y. "Flow-induced vibration of two circular cylinders in tandem arrangement part 2: suppression of vibrations." *Journal of Wind Engineering and Industrial Aerodynamics* 97 (2009): 312-319.
70. Kim, S., Alam, M.M., Sakamoto, H., Zhou, Y. "Flow-induced vibrations of two circular cylinders in tandem arrangement. Part 1: characteristics of vibration." *Journal of Wind Engineering and Industrial Aerodynamics* 97 (2009): 304-311.
71. King, R. "A review of vortex shedding research and its application." *Ocean Energy* 4 (1977): 141-171.
72. Klamo, J.T., Leonard, A., Roshko, A. "The effects of damping on the amplitude and frequency response of a freely vibrating cylinder in cross-flow." *Journal of Fluid and Structures* 22 (2006): 845-856.
73. Kumar R.A., Sohn, C.H., Gowda, B.H.L. "Influence of corner radius on the near wake structure of a transversely oscillating square cylinder." *Journal of Mechanical Science and Technology* 23 (2009): 2390-2416.

74. Lakshmana B.H., Gowda, Prabhu D.R. "Interference effects on the flow-induced vibration of a circular cylinder." *J.Sound & Vibration* 112 (1987): 487-502.
75. Lee J.H., Bernitsas M. M. "High-Damping, High-Reynolds VIV Tests for Energy Harnessing Using the VIVACE Converter." *Ocean Engineering*, February 2010.
76. Lee J.H., Chang C. C. (Jim), Xiros N., Bernitsas M. M. "Integrated Power Take Off and Virtual Oscillator System for the VIVACE Converter: Vck Syastem Identification." 2009 ASME International Engineering Congress and Exposition. Lake Buena Vista, FL, 2009. 13-19.
77. Lee J.H., Xiros N., Bernitsas M. M. "Virtual Damper-Spring System for VIV experiments and Hydrokinetic Energy Conversion." *Ocean Engineering*, 2009.
78. Lee, J. "Hydrokinetic power harnessing utilizing vortex induced vibrations through a virtual c-k VIVACE model." 2009.
79. Lin, J.C. Towfighi, J. Rockwell, D. "Instantaneous structure of the near-wake of a circular cylinder: on the effect of Reynolds Number." *Journal of Fluids & Structures* 9, no. 4 (1995): 409.
80. Macdonald, J.H.G., Larose, G.L. "Two-degree-of-freedom inclined cable galloping part 1: general formulation and solution for perfectly tuned system." *Journal of Wind Engineering* 96 (2008): 291-307.
81. Marakkos, K., Turner, J.T. "Vortex generation in the cross-flow around a cylinder attached to an end-wall." *Optics and Laser Technology* 38 (2006): 277-285.
82. Morse, T.L., Williamson C.H.K.,. "Prediction of vortex-induced vibration response by employing controlled motion." *Journal of Fluid Mechanics* 634 (2009): 5-39.
83. Nakamura, K., Hirata, K, Urabe, T. "Galloping of rectangular cylinders in the presence of a splitter plate." *Journal of Fluids and Structures* 5 (1991): 521-549.
84. Nakamura, Y., and Tomonari, Y. "The effects of surface roughness on the flow past circular cylinders at high Reynolds numbers." *Journal of Fluid Mechanics* 123, no. 1 (1982): 363-378.
85. Nakamura, Y., Hirata, K., and Kashima, K. "Galloping of a circular cylinder in the presence of a splitter plate." *Journal of Fluids and Structures* 8 (1994): 355-365.
86. Naudascher, E., Weske, J.H., Fey, B. "Exploratory study on damping of galloping vibrations." *Journal of Wind Engineering and Industrial Aerodynamics* 8 (1981): 211-111.
87. Noui-Mehidi, M.N. "Effect of acceleration on transition properties in a conical cylinder system." *Experimental Thermal and Fluid Science* 29 (2005): 447-456.
88. Oudheusden, B.W.V., Scarano, F., Hinsberg, N.P.V., Roosenboom, E.W.M. "Quantitative visualization of the flow around a square-section cylinder at incidence." *Journal of Wind Engineering and Industrial Aerodynamics* 96 (2008): 913-922.
89. Parkinson, G.V., Sullivan, P.P. "Galloping response of towers." *Journal of Industrial Aerodynamics* 4 (1979): 253-260.

90. Parkinson, G.V., Wawzonek, M.A. "Some considerations of combined effects of galloping and vortex resonance." *Journal of Wind Engineering and Industrial Aerodynamics* 8 (1981): 135-143.
91. Raghavan K., Bernitsas M. M. "Enhancement of High Damping VIV through Roughness Distribution for Energy Harnessing at $8 \times 10^3 < Re < 1.5 \times 10^5$." OMAE'08 Conf. Estoril, Portugal.
92. Raghavan K., Bernitsas M. M. "Experimental Investigation of Reynolds Number Effect on Vortex Induced Vibration of Rigid Cylinder on Elastic Supports." *Ocean Engineering*, 2010.
93. Raghavan K., Bernitsas M. M., Maroulis D. "Effect of Bottom Boundary on VIV for Energy Harnessing at $8 \times 10^3 < Re < 1.5 \times 10^5$." *Journal of Offshore Mechanics and Arctic Engineering*, ASME Transactions 131, no. 3 (2007): 031102.
94. Raghavan K., Bernitsas M. M., Maroulis D. "Effect of Reynolds Number on Vortex Induced Vibrations." IUTAM Symposium. Hamburg, Germany, 2007.
95. Raghavan, K. "Energy extraction from a steady flow using vortex induced vibration." 2007.
96. Raghavan, K., and Bernitsas, M. M. "Enhancement of high damping VIV through roughness distribution for energy harnessing at $8 \times 10^3 < Re < 1.5 \times 10^5$." Fifth Conference on Bluff Body Wakes and Vortex-Induced Vibrations. Costa do Sauipe, Bahia, Brazil.
97. Sarpkaya, T. "A critical review of the intrinsic nature of vortex induced vibrations." *Journal of Fluids and Structures* 19(4) (2004): 389-447.
98. Sarpkaya, T. "Vortex-induced oscillations: a selective review." *Journal of Applied Mechanics*, no. 46 (1979): 241-257.
99. Sarpkaya, T. "Vorticity, free surface, and surfactants." *Annual Reviews of Fluid Mechanics* 28 (1996): 83-128.
100. Schlichting, H. *Boundary Layer Theory*. 7th. Springer-Verlag Berlin Heidelberg.
101. Shih W.C.L., Wang C., Coles D., A. Roshko. "Experiments on flow past rough circular cylinders at large Reynolds numbers." *J. Wind Engng. and Industrial Aerodynamics* 49 (1983): 351-368.
102. Sumner D., Price S.J. Paidoussis M.P. "Flow-pattern identification for two staggered circular cylinders in cross flow." *J. Fluid. Mechanics* 411: 263-303.
103. T., Sarpkaya. "Hydrodynamic damping, flow induced oscillations and biharmonic response." *ASME J. Offshore Mech. Arctic Engng* 177 (1995): 232-238.
104. Takeuchi, T., Matsumoto, M. "Aerodynamic response characteristics of rectangular cylinders in tandem arrangement." *Journal of Wind Engineering and Industrial Aerodynamics* 41-44 (1992): 565-575.
105. Tamura, T., Dias, P.P.N.L. "Unstable aerodynamic phenomena around the resonant velocity of a rectangular cylinder with small side ratio." *Journal of Wind Engineering and Industrial Aerodynamics* 91 (2003): 127-138.

106. Thorpe, T.W. "An overview of wave energy technologies." *An Overview of Wave Energy Technologies*, 1998.
107. Triantafyllou, Hover F.S. and M.S. "Combined simulation and real-time force feedback: A new tool for experimental fluid mechanics", in *System Theory: Modeling, Analysis and Control*. Edited by Irvin Schick T. Tzaferis. Kluwer Academic Publishers, 1999.
108. W.H., Cheung J.C.K. and Melbourne. "Turbulence effects on some aerodynamic parameters of a circular cylinder at supercritical Reynolds numbers." *Wind Engng. Industrial Aerod.* 14 (1983): 399-410.
109. Wacker, J., Friedrich, R., Plate, E.J., Dorsch, F. "Drag and lift on rectangular bluff bodies immersed in deep boundary layer flow over rough surfaces." *Journal of Wind Engineering and Industrial Aerodynamics* 33 (1990): 113-122.
110. Walker, D.T., Lyzenga D.R., Ericson, E.A. and Lund, D.E. "Radar backscatter and surface roughness measurements for stationary breaking waves." *Royal Society - Mathematical, Physical and Engineering Sciences (Series A)*. 1996. 1953-1984.
111. WaveNet. "Results from the work of the European Thematic Network on Wave Energy." European Community, 2003.
112. Williamson C.H.K, Govardhan R. "Vortex induced vibrations." 36 (2004): 413-455.
113. Williamson C.H.K, Roshko A. "Vortex formation in the wake of an oscillating cylinder." *J. Fluids Structures* 2 (1988): 355-381.
114. Williamson, C.H.K. "Vortex dynamics in the cylinder wake." *Annual Review of Fluid Mechanics* 28 (1996): 477-539.
115. Williamson, C.H.K., Roshko, A. "Vortex formation in the wake of an oscillating cylinder." *Journal of Fluids and Structures* 2 (1988): 355-381.
116. WMCE. "Ocean Energy Systems, Status and Research and Development Priorities in Wave and Marine Current Energy." 2003.
117. Xiao, S., Wu, J. "Simulation and effects evaluation of anti-galloping devices for overhead transmission lines." 4th IEEE Conference on Automation Science and Engineering. Washington DC, USA, 2008. 808-813.
118. Xu, S.J., Zhou, Y., Wang, M.H. "A symmetric binary-vortex street behind a longitudinally oscillating cylinder." *Journal of Fluid Mechanics* 556 (2006): 27-43.
119. Zan S.J., Matsuda and K. "Steady and unsteady loading on a roughened circular cylinder at Reynolds numbers up to 900,000." *J. Wind Engng. and Industrial Aerodynamics* 90 (2002): 567-581.
120. Zdero, R., Turan, O.F., Havard, D.G. "Toward understanding galloping: near-wake study of oscillating smooth and stranded circular cylinders in forced motion." *Experimental Thermal and Fluid Science* 10 (1995): 28-43.
121. Zdravkovich, M. M. "Conceptual overview of laminar and turbulent flows past smooth and rough circular-cylinders." *Journal of Wind Engineering and Industrial Aerodynamics* 33 (1990): 53-62.

122. Zdravkovich, M.M. Flow around circular cylinders Vol.1: Fundamentals. Edited by Achenbach E. Oxford Science Publishers, 1997.
123. Zdravkovich, M.M. "Flow induced oscillations of two interfering circular cylinders." *J.Sound & Vibration* 101(4) (1985): 511-521.
124. Zdravkovich, M.M. "Review and classification of various aerodynamic and hydrodynamic means for suppressing vortex shedding." *J.Wind Engineering & Industrial Aerodynam* 7 (1981): 145-189.
125. Zhou Y., Feng S.X., Mahbub Md. A., Bai, H.L. "Reynolds number effect on the wake of two staggered cylinders." *Physics of Fluids* 21 (2009): 125105-1 to 125105-14.